Crustal structure of Mars from gravity and topography

G. A. Neumann,[1,2] M. T. Zuber,[1,2] M. A. Wieczorek,[3] P. J. McGovern,[4] F. G. Lemoine,[2] and D. E. Smith[2]

[1]   Mars Orbiter Laser Altimeter (MOLA) topography and gravity models from 5 years of Mars Global Surveyor (MGS) spacecraft tracking provide a window into the structure of the Martian crust and upper mantle. We apply a finite-amplitude terrain correction assuming uniform crustal density and additional corrections for the anomalous densities of the polar caps, the major volcanos, and the hydrostatic flattening of the core. A nonlinear inversion for Moho relief yields a crustal thickness model that obeys a plausible power law and resolves features as small as 300 km wavelength. On the basis of petrological and geophysical constraints, we invoke a mantle density contrast of 600 kg m^{-3}; with this assumption, the Isidis and Hellas gravity anomalies constrain the global mean crustal thickness to be >45 km. The crust is characterized by a degree 1 structure that is several times larger than any higher degree harmonic component, representing the geophysical manifestation of the planet's hemispheric dichotomy. It corresponds to a distinction between modal crustal thicknesses of 32 km and 58 km in the northern and southern hemispheres, respectively. The Tharsis rise and Hellas annulus represent the strongest components in the degree 2 crustal thickness structure. A uniform highland crustal thickness suggests a single mechanism for its formation, with subsequent modification by the Hellas impact, erosion, and the volcanic construction of Tharsis. The largest surviving lowland impact, Utopia, postdated formation of the crustal dichotomy. Its crustal structure is preserved, making it unlikely that the northern crust was subsequently thinned by internal processes.   *INDEX TERMS:* 1227 Geodesy and Gravity: Planetary geodesy and gravity (5420, 5714, 6019); 5420 Planetology: Solid Surface Planets: Impact phenomena (includes cratering); 5410 Planetology: Solid Surface Planets: Composition; 5415 Planetology: Solid Surface Planets: Erosion and weathering; 5430 Planetology: Solid Surface Planets: Interiors (8147); *KEYWORDS:* crustal dichotomy, impact basins, Martian crust

1.   Introduction

[2]   The first reliable model of the structure of the crust and upper mantle of Mars from remote observations was produced by *Zuber et al.* [2000] using data from the Mars Orbiter Laser Altimeter (MOLA) and the Radio Science investigation of the Mars Global Surveyor (MGS) spacecraft. *Zuber et al.* [2000] assumed a uniform crustal density and solved for the global variations in crustal thickness using a gravity field derived from preliminary MGS tracking [*Smith et al.*, 1999a]. In that study, spherical harmonic potential coefficients were derived to degree and order 80, but crustal structure was interpreted cautiously to degree 60, or 360 km wavelength, owing to the presence of noise. Tracking normal equations have since been generated to degree 75 [*Yuan et al.*, 2001], to degree 80 (supplemented by altimetric crossovers) [*Lemoine et al.*, 2001], 85 [*Tyler et al.*, 2002], and higher [*Tyler et al.*, 2003, 2004], using new constants for the rotation rate and the orientation of the Martian spin pole provided by the IAU2000 rotation model [*Folkner et al.*, 1997; *Seidelmann et al.*, 2002]. Gravity models now incorporate tracking data coverage from the Primary and Extended MGS missions and the early phases of the Mars Odyssey mission. In the present study we exploit these advances in gravity modeling to present a refined crustal inversion, which we also interpret in the context of Mars' thermal evolution.

[3]   Volcanic constructs and giant chasms generate significant power in the gravity signal at wavelengths as short as 250 km, or degree 85 [*Anderson and Grimm*, 1998]. The gravity signal at spacecraft altitudes, stacked over thousands of orbits, is not yet exhausted at degree 85 [*Lemoine et al.*, 2001]. Gravity anomalies at these wavelengths are similar in spatial scale to many craters and basins, and when

[1]Department of Earth, Atmospheric and Planetary Sciences, Massachusetts Institute of Technology, Cambridge, Massachusetts, USA.
[2]Laboratory for Terrestrial Physics, NASA Goddard Space Flight Center, Greenbelt, Maryland, USA.
[3]Département de Géophysique Spatiale et Planétaire, Institut de Physique du Globe de Paris, Paris, France.
[4]Lunar and Planetary Institute, Houston, Texas, USA.

combined with topography, contain information about the response of the crust to bolide impacts [*Melosh*, 1989]. Higher resolution of crustal structure than obtained by *Zuber et al.* [2000] is now feasible. To the extent that recent high-degree potential models exhibit statistical power-law behavior and are coherent with topography, we apply topographic corrections to obtain a Bouguer anomaly.

[4] Earlier studies [*Phillips et al.*, 1973; *Bills and Ferrari*, 1978; *Frey et al.*, 1996; *Kiefer et al.*, 1996] used spherical harmonic gravity and topographic data sets of relatively low degree. Long-wavelength errors up to 5 km in the topography [*Smith et al.*, 1999b] hindered the early interpretations. Potential coefficients to degree and order 50 were derived from reanalysis of Viking and Mariner spacecraft tracking using a power-law constraint [*Smith et al.*, 1993; *Konopliv and Sjogren*, 1995], although the coefficient uncertainty exceeded signal above degree 30. With tracking below 500 km available only at $40°S–50°N$, these fields had poor resolution in the polar regions, and could only partially resolve the gravity signature of first-order topographic features such as the equatorial mountains and the highland-lowland boundary.

[5] A roughly hemispheric Martian dichotomy [*Mutch et al.*, 1976; *Carr*, 1981] between the smooth northern lowlands and the rougher southern highlands has been defined in terms of differences in elevation and surface cratering age. Lacking accurate topography the relationship of the geological dichotomy to crustal structure was unclear. Some of the dichotomy boundary coincides with the margins of the Hellas and Isidis impacts, and part of the lowlands could be identified with the Utopia Basin [*McGill*, 1989], but direct evidence for an impact origin was lacking. Using remote radar soundings and radio occultations, *Smith and Zuber* [1996] characterized the topographic dichotomy by a pole-to-pole slope represented by a displacement of 3 km between the center of figure and the center of mass. Early MOLA topography revealed a $2–4$ km scarp along some parts of the boundary, similar to terrestrial passive margins [*Frey et al.*, 1998].

[6] Martian topography [*Smith and Zuber*, 1996; *Smith et al.*, 1999b, 2001b] was found to be bimodal when measured about the planetary center of mass, with peaks at 1.5 km above and 4 km below the datum, but unimodal when measured about the center of figure, suggesting a planetwide redistribution of mass. On the basis of the early studies, several workers postulated a global geophysical dichotomy, or decrease in crustal thickness from south to north, to explain the geological dichotomy [e.g., *Phillips et al.*, 1973; *Bills and Ferrari*, 1978; *Phillips*, 1988].

[7] The first reliable determination of crustal structure using MOLA topography provided further insight into the dichotomy [*Zuber et al.*, 2000; *Zuber*, 2001]. *Zuber et al.* [2000] inverted a Bouguer potential anomaly by downward-continuation to a crust-mantle interface at a prescribed depth of 50 km below the reference equatorial radius of 3396 km. This work showed that the crustal dichotomy only partially coincides with the topographic and geologic boundary between the older, heavily cratered southern highlands and the resurfaced northern lowlands, but does correlate with global-scale, thermally mapped compositional differences [*Bandfield et al.*, 2000].

[8] The model of *Zuber et al.* [2000] varied from a minimum of 3 km to a maximum of 92 km thickness, with the northern lowlands characterized by a relatively uniform 35-km-thick crust. The crustal thickness, when averaged over the globe, was 43.5 km owing to the flattening of polar topography (not 50 km as stated). The depth of crustal interfaces is not known from seismic measurements, unlike the Earth and Moon, so absolute measurements were constrained by two considerations. First, the amplitude of crust-mantle deflections beneath the Isidis basin did not permit a significantly shallower crust-mantle density interface (Moho). Second, crustal thickness much greater than 50 km was deemed unlikely, as any dichotomy in such a thick crust would have viscously relaxed during Mars' early thermal history [*Zuber et al.*, 2000; *Nimmo and Stevenson*, 2000].

[9] *Zuber et al.* [2000] neglected the lower density of the polar ice caps [*Johnson et al.*, 2000], the higher density of the Tharsis volcanoes [*McGovern et al.*, 2002], and the flattening of the core-mantle boundary [*Folkner et al.*, 1997; *Yoder et al.*, 2003]. We apply these additional corrections based on inferred compositions. The residual anomaly is then filtered and inverted using the finite-amplitude method of *Wieczorek and Phillips* [1998] to resolve thickness variations at wavelengths of 300 km. The inferred Moho shape has a power-law behavior matching that of the surface.

2. Data

[10] In this section we describe the topography, gravity, and assumed density values used in the inversion, as well as caveats associated with these models and parameters that bear on the final results.

2.1. Topography and Reference Surfaces

[11] Topography of Mars has been obtained by the Mars Orbiter Laser Altimeter (MOLA) [*Zuber et al.*, 1992; *Smith et al.*, 2001b], which measured the planetary radius at ∼600 million locations. Unique among planets, the shape of Mars about its center of mass is known globally at meter-level accuracy [*Neumann et al.*, 2001]. Cartographers describe positions on Mars with reference to an ellipsoid with mean equatorial and polar radii of 3396.19 km and 3376.2 km respectively [*Seidelmann et al.*, 2002]. Geophysicists, however, often adopt a spherical datum of radius $R = 3396$ km for modeling the gravitational attraction of surface relief. More properly termed the planetary shape, we will refer to the deviations h of planetary radius from this sphere as topography, with nearly equal minimum and maximum excursions (23 and 21 km). The mean planetary radius $R_{mean} = 3389.500$ km represents the equivalent spherical planetary volume and is significantly less than the equatorial radius used as a reference radius in this work. To reduce dynamic range and to discuss topographic loading, as we do in section 5, planetary elevations may also be referenced to an equipotential surface, or areoid. Where necessary to avoid confusion, the term "equipotential topography" will be used for elevations about an areoid whose mean radius at the equator is 3396 km. This areoid is determined by satellite tracking and departs by up to 2 km from an ellipsoid of revolution.

[12] The binned MOLA radius data "megr90n000eb. img" may be obtained from the Planetary Data System [*Smith et al.*, 2003]. We average the four pixels adjacent to grid points at even spacings of 1/8° longitude and latitude to obtain an N_{lon} = 2881 by N_{lat} = 1441 array $h(i, j)$, identifying data at 0 and 360°. The discrete-Fourier-transformed [*Oppenheim and Schafer*, 1975] topography $H_j(m)$ at latitude index j is thereby in phase with the spherical harmonics of order m.

[13] We represent topography in spherical harmonics as

$$h(\phi, \lambda) = \sum_{l=0}^{\infty} \sum_{m=0}^{l} P_{lm}(\sin \phi)[A_{lm} \cos(m\lambda) + B_{lm} \sin(m\lambda)], \quad (1)$$

where ϕ and λ are the areocentric latitude and longitude, P_{lm} are the normalized associated Legendre polynomial functions of degree l and azimuthal order m, and A_{lm} and B_{lm} are the spherical harmonic coefficients. The coefficients are found by suitable integrals over a sphere, owing to the orthogonality of spherical harmonics. For evenly spaced data, the coefficients are approximated by summing $H_j(m)$ times the associated Legendre polynomials weighted proportional to the area associated with a given pixel $\Delta\Omega$ spanning $\Delta\phi = \Delta\lambda = 1/8°$ of latitude and longitude:

$$H_{lm} = \frac{1}{2N_{lon}} \sum_{j=1}^{N_{lat}} H_j(m) P_{lm}[\sin(\phi(j))]\Delta\Omega(j), \quad (2)$$

where the complex spherical harmonic coefficient $H_{lm} = A_{lm} + iB_{lm}$. The weights are

$$\Delta\Omega(j) = [\sin(\phi(j) + \Delta\phi/2) - \sin(\phi(j) - \Delta\phi/2)], \quad (3)$$

while at the poles

$$\Delta\Omega(1) = \Delta\Omega(N_{lat}) = \frac{2}{3}[1 - \cos(\Delta\phi/2)]. \quad (4)$$

The factor of 2/3 reduces the quadrature errors associated with a discrete sum. The weights are normalized to sum to exactly 2. Truncation of this spherical harmonic expansion at degree 90, corresponding to a 4° full wavelength, entails local errors up to ±6.5 km over short-wavelength features in Valles Marineris, but adequately represents the large-scale topographic structure. The root-mean-square (RMS) difference between this expansion and the original topography is 0.4 km.

[14] The spherical harmonic degree variance

$$\sigma_l^2 = \sum_m A_{lm}^2 + B_{lm}^2 \quad (5)$$

may be approximated by an l^{-2} power law on terrestrial planets [*Vening Meinesz*, 1950; *Bills and Kobrick*, 1985], and Mars [*Smith et al.*, 2001b]. Anticipated variations in height of shallow density interfaces would plausibly obey a similar power law, scaled by the density contrast required for local compensation.

2.2. Gravity

[15] The static gravitational potential of a planetary body at distance r from its center is expressed in spherical harmonics [*Kaula*, 1966]

$$U(r, \phi, \lambda) = \frac{GM}{r}\left[1 + \sum_{l=1}^{\infty}\left(\frac{R}{r}\right)^l \sum_{m=0}^{l} P_{lm}(\sin\phi)\text{Re}\left(U_{lm}e^{-im\lambda}\right)\right], \quad (6)$$

where G is Newton's constant of gravitation, M is the total planetary mass, R is the reference equatorial radius, and $U_{lm} = C_{lm} + iS_{lm}$. Whereas the degree 1 coefficients are identically 0 in a center-of-mass coordinate system, the anomalous potentials arising from perturbations of the surface and internal density interfaces may have non-zero offsets from the center of mass.

[16] The largest anomalous potentials arise from surface topography and shallow interfaces like that between crust and mantle, although density variations within the crust may also contribute [*Arkani-Hamed*, 2000; *Arkani-Hamed and Riendler*, 2002]. The flattening of the core-mantle interface contributes a small ellipsoidal component. Additional long-wavelength anomalies may arise from dynamically maintained internal density variations in a viscous convecting mantle [*Kiefer et al.*, 1996; *Harder and Christensen*, 1996; *Defraigne et al.*, 2001], although on a planet with a thick lithosphere these are thought to be small [*Zhong*, 2002].

[17] The potential anomaly arising from topography may be calculated to first order [*Esposito et al.*, 1992] assuming a crust of uniform density ρ_c and a mean density $\bar{\rho}$ (for simplicity, the planetary mass divided by the volume of a sphere of radius R):

$$U_{lm}^a = \frac{3}{(2l+1)}\frac{\rho_c}{\bar{\rho}}\frac{H_{lm}}{R}. \quad (7)$$

[18] Gravity models obtained primarily from MGS and historical tracking [*Smith et al.*, 1999a; *Lemoine et al.*, 2001; *Yuan et al.*, 2001] are constrained by an empirical power law [*Kaula*, 1966; *Balmino et al.*, 1982] known as Kaula's rule, a consequence of equations (5) and (7). The potential degree variance (as distinct from the topographic σ_l^2 in equation (5)) scales inversely roughly as the cube of the degree (Figure 1a), owing to the factor of $2l + 1$ in equation (7). It is customary to compare the root power per coefficient at degree l:

$$\sigma = \frac{\sigma_l}{\sqrt{(2l+1)}} \quad (8)$$

with a power law of $l^{-1}(2l + 1)^{-1}$, or roughly l^{-2}. Gravity fields estimated from tracking equations use an l^{-2} power law constraint to minimize the covariance of the solution, reducing noise. The formal uncertainty of the solution, derived from the covariance, is thereby reduced, as is the power of the gravity signal at high degrees.

[19] Figure 1a shows the significant reduction in noise in the zonal ($m = 0$) coefficients in the jgm85h02 model compared to earlier models at degrees $l > 50$. The zonal coefficient magnitudes in recent JPL and GSFC solutions often exceeded Kaula's constraint by an order of magnitude at high degrees (Figure 1a) while earlier MGS fields such as mgm0964c20 as used by *Zuber et al.* [2000] were necessarily overconstrained. While the unconstrained
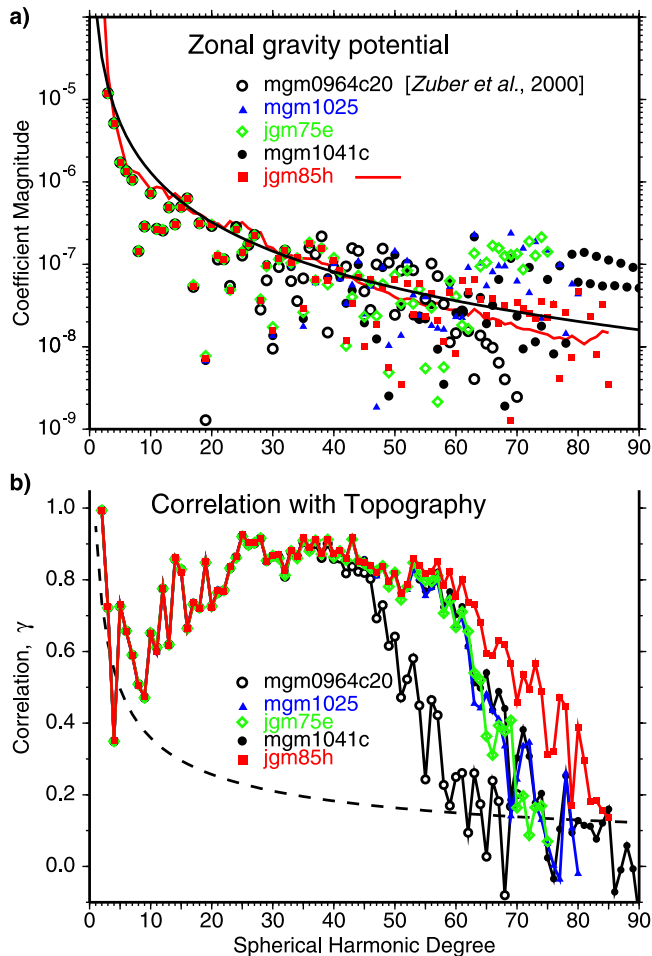
a) Zonal gravity potential

○ mgm0964c20 [*Zuber et al.*, 2000]
▲ mgm1025
◇ jgm75e
● mgm1041c
■ jgm85h ——

b) Correlation with Topography

○ mgm0964c20
▲ mgm1025
◇ jgm75e
● mgm1041c
■ jgm85h

Figure 1. (a) Zonal gravity coefficient magnitudes compared to Kaula's rule for recent MGS gravity field solutions. The degree power is shown for jgm85h02 (red curve). Coefficients diverge from each other and from a power law starting at degree 40. (b) Correlation of gravity fields with topography referenced to a spherical datum. Dashed curve shows 95% confidence level of positive correlation.

coefficient uncertainty of the more recent model mgm1025 is less than the (constrained) coefficient magnitude up to degree 62, the divergence of zonal coefficients starting at degree 40 among the most recent models suggests caution in interpreting the coefficients at higher degrees. The signal in model jgm85h02 exceeds the formal coefficient uncertainty up to degree 72, although the formal uncertainty partly reflects the power law constraint applied from degree 60 onward. Our methods will attempt to resolve some of the signal at degrees 72 and higher.

[20] The degree correlation of gravity with topography, or coherence,

$$\gamma(l) = \frac{\sum_{m=0}^{l} C_{lm} A_{lm} + S_{lm} B_{lm}}{\sqrt{\left(\sum_m C_{lm}^2 + S_{lm}^2\right)\left(\sum_m A_{lm}^2 + B_{lm}^2\right)}}, \quad (9)$$

should approach unity at short wavelengths since such gravity anomalies arise mainly from very localized surface

topographic features such as the Tharsis volcanoes. The portion of the signal in a given field that is linearly related to topography is given by γ, while γ² is the coherence. Figure 1b shows good correlation for all fields up to degree 50, declining at higher degrees, where noise power becomes relatively stronger than signal. At degree 60 or higher, correlation greater than 0.15 is significant at a 95% confidence level. Beyond degree 60, jgm85h02 is more sensitive to topographically induced anomalies than all other fields considered, and γ ≥ 0.15 persists up to degree 85. Model jgm85h02 is more coherent with topography than its predecessor, jgm85f01, and includes 8 months more MGS tracking as well as Mars Odyssey Transition Orbit tracking and an updated rotation model. The analysis of Bouguer gravity will be based on this field.

2.3. Crustal and Mantle Density

[21] The mean density of Mars is 3930 kg m^{-3} [*Smith et al.*, 1999b], considerably less than terrestrial, but the more iron-rich Martian mantle and crust are likely to be denser than Earth's. We assume $\rho_m = 3500$ kg m^{-3} for an olivine upper mantle based on SNC geochemistry [*Sohl and Spohn*, 1997]. Regional densities between 2350 [*McKenzie et al.*, 2002] and 3350 kg m^{-3} [*McSween*, 1985] have been suggested for the rocky crust. *McGovern et al.* [2002] found that $\rho_c = 2900$ kg m^{-3} provided the best fit to localized admittance over much of Mars, if one allows in some places for the presence of subcrustal loading. *Wieczorek and Zuber* [2004] advocate a plausible range of bulk crustal densities from 2700 to 3100 kg m^{-3}. Following many authors, we adopt 2900 kg m^{-3} as a Bouguer reduction density.

[22] The compositions of SNC meteorites provide an additional constraint on the density of the Martian crust. On the basis of elemental abundance data in the Mars Meteorite Compendium (http://curator.jsc.nasa.gov/antmet/ mmc/mmc.htm) for the available Martian meteorites, we have calculated their expected modal mineralogy. The bulk pore-free densities of these samples were then estimated by employing the known densities of their constituent mineral phases. As shown in Table 1, densities of the presumed extrusive basalts (3220 to 3390 kg m^{-3}) are much higher than those typically encountered on the Earth, and in this regard are comparable to those of the lunar mare basalts. The intrusive lherzolites, clinopyroxenites, orthopyroxenites, and dunites are generally believed to be cumulates, and are seen to possess even higher densities. Indeed, Chassigny (a dunite) has a density comparable to that of the Martian mantle. Using a more limited number of samples, *Britt and Consolmagno* [2003] obtained similar results via direct measurements of bulk density and porosity.

[23] Because of the generally young crystallization ages of the Martian meteorites, they are believed to have originated in either the Tharsis plateau or Elysium rise [*McSween*, 1985, 1994]. (On the basis of the ancient age of ALH84001, it is possible that this meteorite might have come from the ancient heavily cratered highlands.) As these two provinces are unique in their long-lived magmatic activity, it is not clear whether samples obtained from these regions should be considered typical of those that make up either the northern lowlands or cratered highlands. Indeed, if the northern lowlands and cratered highlands formed shortly after, or during, the planet's accretion, then the magmatic

Table 1. Pore-Free Rock Densities From Meteorites and in Situ Analysis

Name	Type	Density, kg^{-3}
EETA 79001B	basalt	3220
Los Angeles	basalt	3240
QUE 94201	basalt	3250
Shergotty	basalt	3320
Zagami	basalt	3320
Dhofar 019	basalt	3330
EETA 79001A	basalt	3340
Dar al Gani 476/489	basalt	3360
Sayh al Uhaymir 005/094	basalt	3390
LEW 88516	lherzolite	3400
ALH 77005	lherzolite	3430
Y793605	lherzolite	3430
ALH 84001	orthopyroxenite	3410
Yamato 000593/749	clinopyroxenite	3460
Governador Valadares	clinopyroxenite	3460
Lafayette	clinoproxenite	3480
Nakhla	clinopyroxenite	3480
Chassigny	dunite	3580
MPF APX[a]	"soil-free" rock	3060

[a] As in the work of *Brückner et al.* [2003].

processes responsible for their formation would certainly have been different than those that formed the younger magmatic provinces.

[24] Current orbital remote sensing data sets cannot yet uniquely map the composition of the Martian surface. In situ chemical analyses have been performed during the Viking and Mars Pathfinder (MPF) missions [*Priestley et al.*, 1977; *Rieder et al.*, 1997], and it appears that the composition of rocks at the surface are significantly different than those of the Martian meteorites. Using the chemical composition of the "Mars Pathfinder soil-free rock" as obtained from the Mars Pathfinder Alpha Proton X-ray Spectrometer (APX) [*Brückner et al.*, 2003], we have calculated the modal mineralogy and pore-free density of this hypothetical "rock". Its computed density is 3060 kg m^{-3}, which is considerably less dense than the basaltic Martian meteorites. Martian meteorite porosities are generally about 5% [*Consolmagno and Strait*, 2002; *Britt and Consolmagno*, 2003], but it is not clear if this number is representative of crustal materials on Mars, or if this is instead related to the shock processes during the impact event responsible for ejection of these rocks from the Martian surface. A certain amount of crustal porosity might also be expected if water is present in the subsurface, either as permafrost or in aquifers. Assuming this porosity, the composition of the MPF APX "soil-free rock" is consistent with our assumed average crustal density. This rock is less dense than the SNC's which are believed to have come from Tharsis. While the origin of this rock is uncertain, it is a plausible representative of the cratered uplands of Mars, as Ares Vallis originates in the southern highlands close to the dichotomy boundary and it is possible that this rock was transported from the southern highlands to the Mars Pathfinder landing site.

[25] If the density of the Tharsis volcanoes is greater than that of our chosen average crustal density, as the Martian meteorite data suggest, then considerable error in our crustal thickness inversions could occur beneath these provinces. For this reason we will attempt to take into consideration the likely higher surface densities of the Tharsis and Elysium volcanos. While the density of the surrounding Tharsis plateau is probably greater than typical, it is difficult to constrain the thickness of these ancient high-density materials, and thus we cannot take them into account here.

3. Bouguer Anomaly

[26] Setting aside the central mass (degree 0) term, we separate U into surface and subsurface components:

$$U = U_{crust} + U_{local} + U_{core} + U_{mantle}, \qquad (10)$$

where U_{local} represents isolated crustal density anomalies in an otherwise homogeneous crust. In the following sections we consider contributions from inferred inhomogeneities and from subsurface density interfaces. We calculate U_{crust}, the anomalous potential arising from surface topography, using the higher-order method of *Wieczorek and Phillips* [1998]. To account for finite-amplitude effects, equation (7) is augmented by coefficients applied to the nth powers of topography. These powers are expanded in spherical harmonics using equation (2) up to $n = 6$. Figure 2 shows the similar magnitude of the planetary potential spectrum U (black) and U_{crust} (red). The Bouguer potential U_B should nominally be their difference, $U - U_{crust}$. As a consequence of the decrease in tracking sensitivity at spacecraft altitudes and the a priori power law used to constrain U at degrees higher than 50, this expression tends to overcorrect for gravitational attraction due to topography [*Neumann et al.*, 1996; *Wieczorek and Phillips*, 1998]. Beyond $l = 50$, following *Wieczorek and Phillips* [1998], we set

$$U_B = U - (R/R_f)^{(l-50)} U_{crust}, \qquad (11)$$

where $R_f = R + 100$ km. The amplitude of the filter being applied to U_{crust} closely follows the decline in correlation shown in Figure 1b. The magnitude of the coefficients beyond degree 50 is small, and so the main effect of this filter is to remove high-frequency oscillations or "ringing" in the resulting Bouguer anomaly near the sharpest topographic features. The resulting U_B (Figure 2, green curve) is larger in magnitude than the planetary potential at low degrees owing to local compensation of surface topography. As expected for flexural compensation of surface loads [e.g., *Forsyth*, 1985], $U_B < U$ from degree $14-80$. Without this filter, the Bouguer coefficient root power would exceed U beyond degree 62, increasing the short-wavelength crustal complexity. Beyond degree 80 both spectra are dominated by noise regardless of the filter applied.

[27] The largest single component of the Bouguer anomaly is the degree one zonal term, $U^B_{1,0}$, which represents a mass excess in the northern hemisphere and a corresponding mass deficit in the southern hemisphere. The next largest terms are $U^B_{2,0}$, corresponding to the flattening of the planet, and $U^B_{2,2}$, corresponding to the Tharsis bulge.

[28] Figure 3 shows the Bouguer anomaly without the degree 1 and 2 terms. The Isidis, Argyre, Utopia and Hellas basins have large positive circular anomalies (but not some other putative basins such as Daedalia [*Craddock et al.*, 1990], Elysium [*Schultz et al.*, 1982] and North Tharsis [*Schultz and Frey*, 1990] thought to underlie the northern lowland plains). Such Bouguer mass excesses arise from
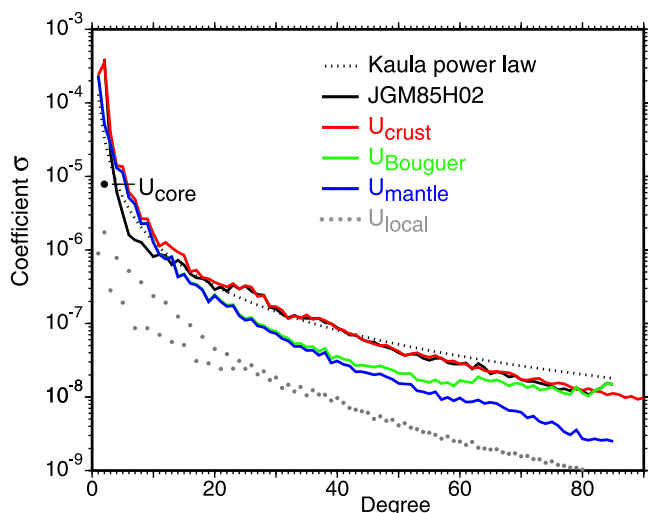
Figure 2. Spectrum of gravity field components.

uplift of Moho following impact [e.g., *Neumann et al.*, 1996] and subsequent modification by volcanic and sedimentary surface loads [e.g., *Buczkowski and McGill*, 2003; *Buczkowski and Cooke*, 2004]. Smaller positive anomalies are associated with Ares Vallis, Chryse and Amazonis, features that might have resulted from one or more early impacts [*Frey and Schultz*, 1988; *Schultz and Frey*, 1990; *Frey*, 2003]. Such anomalies lack a clear circular form in the Bouguer map. The Ladon basin at 330°E, 18°S and the 570-km-diameter crater Mangala at 210°E, 2°N [*Frey and Schultz*, 1988] are roughly circular anomalies, and there is a suggestion of a similar-sized crater "NWO" at 220°E, 28°N, northwest of Olympus Mons and buried by aureole deposits [*McGovern*, 2002]. Some 300-km-diameter craters such as Newton and Copernicus (190–200°E, 40–50°S) have distinct positive anomalies, although somewhat larger ones like Schiaparelli, Cassini, and Huygens have little or none. Several enigmatic positive anomalies not associated with either topographic or geological features appear in the northern circumpolar lowlands. Anomalies such as that at 63°E, 71°N, here designated "E-NE", indicate buried structures of 600 km or more in extent in the northern lowlands that predate both the visible geological record and the early-Noachian buried surface described by *Frey et al.* [2002].

[29] Kasei Valles and parts of Coprates and Eos Chasma have substantial positive anomalies, suggesting that these topographic depressions are underlain by shallower mantle or crustal intrusions, while Ius and Capri Chasma do not, possibly owing to the limited resolution of the gravity field. The Bouguer map shows no indication of linear negative anomalies in Acidalia Planitia, once thought to be associated with buried channels [*Zuber et al.*, 2000; *Phillips et al.*, 2001]. Such troughs are observed in the free-air gravity field [*Smith et al.*, 1999a] and it has been proposed that they represent an edge effect of compensated topography at the highland-lowland boundary [*Dombard et al.*, 2004]. We shall examine these below in the light of an inversion for mantle relief.

[30] Alba Patera, Tempe Terra, and the Elysium rise exhibit highly negative Bouguer anomalies, as expected

for compensation of mountains by thicker and/or lower density crust. Alba Patera and Elysium have been found to have similar gravity/topography admittances [*McGovern et al.*, 2002]. Negative anomalies also characterize the broad highlands such as Hesperia Planum surrounding Hellas, and the Noctis, and Claritis Fossae situated atop the Tharsis rise.

3.1. Mantle and Core Flattening

[31] Mars' core is denser than its mantle and contributes to the degree 2 zonal harmonic potential. We do not consider contributions to the Bouguer anomaly from mantle convection and dynamic core-mantle topography, which are thought to be small [*Zhong*, 2002] and cannot be uniquely constrained from gravity and topography. While the gravitational potential contains a large degree 2 term arising from the rotational flattening of the planet as a whole, the topographic flattening is similar in magnitude and accounts for most of C_{20}. The hydrostatic flattening of the core-mantle boundary also contributes to degree 2. *Folkner et al.* [1997] and *Yoder et al.* [2003] estimate core radii R_C in the range 1520–1840 km. Their models imply that R_C/R ranges from 0.45 to 0.54, with densities from 5200–7500 kg m^{-3}. The mass of the core therefore ranges from 0.15 to 0.21 M, and the mass excess of the core due to its greater density ranges from 0.06–0.09 M. Assuming the same degree of flattening of the core as that of the planet as a whole, such a mass fraction will contribute proportionally to the zonal potential, but by equation (6), the degree 2 potential at radius R will be scaled by the factor $(R_C/R)^2$, or about 0.2–0.3. Thus approximately 1–3% of the degree 2 potential arises from the density contrast at the core-mantle boundary. We set U_{core} to a nominal 2% of $C_{2,0}$ (Figure 2).

3.2. Volcanic Density Anomalies

[32] Olympus Mons and the Tharsis Montes are volumetrically the largest volcanoes and produce the largest positive free-air gravity anomalies in the solar system. They have positive Bouguer signatures at a scale of ~300 km (Figure 3). Alba Patera, as a volcanic rise, is similar in volume to Olympus Mons but differs markedly in profile and has a negative Bouguer signature. A slight increase in Bouguer anomaly near the center of Elysium Mons is disguised by the broader negative anomaly associated with the Elysium rise. If these volcanos were flexurally compensated, the expected Bouguer anomaly would be negative, in contrast to what is observed. A positive signal would be expected, however, if the density of the volcano was greater than that used when calculating the gravity due to the surface topography. The actual distribution of excess mass cannot be uniquely determined from gravity, and could lie deeper, but an unusually cold, dense, or uplifted underlying mantle seems less likely than a positive near-surface density anomaly. *McGovern et al.* [2002, 2004] suggested that the major domical edifices of Tharsis are denser than our average 2900 kg m^{-3} crustal density, although their analyses represented averages over a broader region than a single volcano. *Kiefer* [2004] inferred local densities exceeding 3300 kg m^{-3} in extinct magma chambers underlying shallower volcanoes such as Nili Patera, where there is a small positive anomaly.

[33] We model these local short-wavelength anomalies via near-surface placements of higher-density material, using a
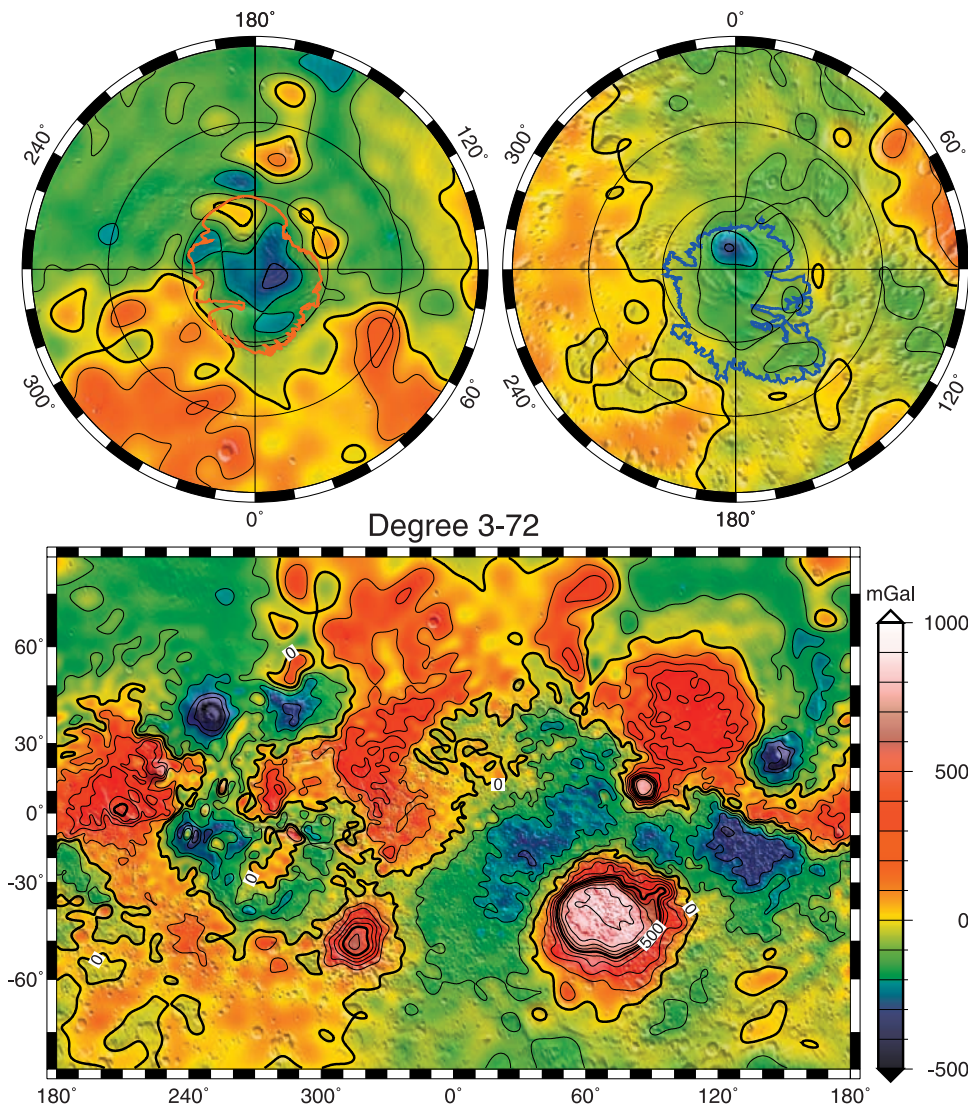
Figure 3. Color-contoured map of Bouguer anomaly, in Mercator (−75 to 75°) and polar stereographic (60–90°N, left; 60–90°S, right) projections, with shaded relief map for context. Contour interval is 100 mGal. Degree 1 and degree 2 terms are omitted. Outlines of the polar layered terrain are shown in polar projections.

value typical of the intrusive rocks in Table 1, reduced somewhat to account for porosity. Elysium Mons and the Tharsis volcanos are assigned a value of 3300 kg m^{-3} [*McGovern et al.*, 2004], in the manner given in Table 2.

[34] We define the extent of the additional mass concentrations in a geometric fashion, without attempting to resolve the volcanic structure in detail. The base of each mountain in Table 2 lies at an elevation that approximates the surrounding terrain, while the outline of each mountain is defined by a closed elevation contour slightly higher than the surrounding terrain, to avoid including distal deposits. The volume assigned a higher density lies between the base and the surface, and within the area defined by the outline contour.

[35] For convenience we apply the anomalous mass as a topographic increase when calculating U_{crust}, effectively placing the extra mass at the surface. While the finite-amplitude calculation of U_{local} could be performed in the same fashion as for the surface topography, the surface

mass placement is a conservative approximation, given the limited resolution and overall uncertainty in our model, minimizing the excess mass required. All told, roughly 1.7×10^{18} kg is added.

3.3. Polar Anomalies

[36] In Figure 3, Bouguer anomalies are negative over both poles. The polar layered terrains, up to 3 km thick [*Zuber et al.*, 1998; *Smith et al.*, 1999b], are less dense than rocky crust and are overcorrected in equation (10) by U_{crust}. The North Polar Cap is surrounded by a surface with very low relief, conforming to a flexural moat adjacent to the Tharsis rise [*Phillips et al.*, 2001]. To estimate its volume, we fit a cubic surface to the northern plains in stereographic projection, omitting the cap, and continue this surface beneath the polar equipotential topography. A contour at an average level of −4400 m encloses most of the layered terrains and the dune-covered Olympia lobe, thought to be

Table 2. Model Area, Volume, and Excess Mass of Martian Volcanos

Name	Base[a]	Outline[b]	Area[c] $\times 10^9$	Volume[c] $\times 10^{12}$	Mass[c] $\times 10^{15}$
Elysium	500	2000	87.75	296.7	118.7
Olympus	1000	2500	255.36	2,253.3	901.3
Ascraeus	6000	7500	87.70	487.6	195.0
Pavonis	6000	7500	98.01	358.4	143.4
Arsia	6000	9000	120.18	825.7	330.3

[a]Elevation, m, above which higher density is applied.
[b]Level of enclosing contour, m.
[c]In SI units.

part of the residual cap [*Fishbaugh and Head*, 2000]. The volume between the trend surface, at a mean depth of −4900 m, and the topographic surface enclosed by this contour is 1.15×10^9 m^3. If the layered terrains are regionally compensated by flexure of a 120-km-thick lithosphere [*Johnson et al.*, 2000], their volume could be 25–50% greater [*Smith et al.*, 1999b].

[37] In correcting for the polar loads, we consider only the volume of the polar ice emplaced above the trend of the surrounding plains, as the polar gravity signals are complex and the signature of partially compensated surface loads is poorly resolved. Relaxation of lithosphere and mantle under such loads takes place over time scales of 10^5–10^7 years [*Johnson et al.*, 2000], comparable to that of changes in obliquity of the polar axis, and accordingly changes in climate [*Kieffer and Zent*, 1992; *Touma and Wisdom*, 1993]. The caps are geologically young, and isostatic adjustment to changing loads may therefore be incomplete.

[38] The southern layered terrains grade downhill, merging into the surrounding cratered highlands, but appear to have been emplaced on a 1–2 km high plain marked by Schmidt Valley, Prometheus Basin, and the Dorsa Argentia formation [*Head and Pratt*, 2001; *Fishbaugh and Head*, 2001]. The South Polar Cap is here defined by a contour at 2000 m elevation and a base lying near the 1200-m floor of Prometheus Basin. The volume enclosed is roughly 1.58×10^9 m^3. The polar caps, composed mainly of H$_2$O ice coated with a thin layer of CO$_2$ ice and dust, have densities approaching that of water ice [*Smith et al.*, 1999b, 2001a]. The local anomaly is calculated at both poles on the basis of a density of 1000 kg m^{-3}.

[39] The density difference between the global crustal density assumed and the polar ice is applied as a reduction in topography when calculating the terrain correction. With these local corrections (Figure 2, gray curve), the residual Bouguer potential variance at high degrees is reduced, as expected for nearly uncompensated loads. The implications of such local density variations for the shape of the crust-mantle interface will be examined in section 5.2.

4. Potential Inversion

[40] The residual Bouguer potential not accounted for by local shallow density anomalies and core flattening is $U_{RB} = U_B - U_{local} - U_{core}$. We solve for undulations of the mantle at the Moho that match the residual anomaly. To first order, in the absence of noise, this is a downward continuation to an average crust-mantle interface depth. Modifications to account for finite-amplitude topography and noise are discussed below. We assume a crust-mantle interface at a

mean radius $R_{cm} = R_{mean} - 45$ km $= R - 51.5$ km, or 45 km less than the mean planetary radius.

4.1. Mean Crustal Thickness

[41] There are no direct measurements of the thickness of the Martian crust, so the interface depth must be assumed. *Sohl and Spohn* [1997], using geochemical arguments, estimated mean crustal thicknesses in the range of 100–250 km. *Norman* [1999] found that less than 45 km of crust could be geochemically enriched. Viscous relaxation arguments [*Zuber et al.*, 2000; *Nimmo and Stevenson*, 2001] suggest that 50–100 km is the maximum thickness that could maintain hemispheric crustal variations against channel flow over Martian history. Using line-of-sight accelerations, *Nimmo* [2002] inferred a thickness upper bound across the dichotomy boundary of 75 km, equivalent to a 55-km global average, while *Wieczorek and Zuber* [2004] suggest a 50 ± 12-km average thickness on the basis of a combination of several geophysical and geochemical studies. *Turcotte et al.* [2002] found higher (>90 km) crustal thickness surrounding the Hellas basin, but used a Cartesian approximation not referenced to the center-of-mass and neglected the non-Airy flexural signature of Tharsis. Following *Zuber et al.* [2000], we use a mean thickness of 45 km, consistent with global density models of large impact basins, as discussed below.

4.2. Finite Amplitude Inversion

[42] The residual Bouguer potential is modeled using the method of *Wieczorek and Phillips* [1998] to solve for the Moho relief, which takes into account the significant finite-amplitude effects [e.g., *McGovern et al.*, 2002]. This method iteratively recalculates the mantle topographic model that matches U_{RB} [*Wieczorek and Phillips*, 1998, equation 18]. Convergence to a unique solution may require under-relaxation to avoid oscillations.

[43] Such solutions amplify the high degree terms roughly as ξ^{-l}, where $\xi = R_{cm}/R$. The Bouguer potential spectrum departs from power-law behavior at degrees >40 (Figure 2) and is undoubtedly contaminated by noise. Modeling this noise by undulations of the Moho would require unphysically large amplitudes. An approach taken by several workers [e.g., *Phipps Morgan and Blackman*, 1993] has been to minimize some norm of the complexity of the solution, which amounts to a filter in transform space. Such a filter should be unity at long wavelengths and should approach zero where the observed gravity field is not determined.

[44] Lacking more specific constraints, we assume that the degree variance spectrum of the Moho relief should resemble that of the surface topography. We apply a factor of $[1 + \exp((l - 63)/12.5))]^{-1}$ to U_{RB}. The magnitude of this filter is 50. It ensures that the power spectrum of the inverted Moho shape resembles that of the topography, scaled by the density contrast. The model for crustal thickness follows (within a factor of two) a power law to degree and order 85. Crustal thickness is chiefly controlled by mantle topography, but where the surface relief is pronounced, as with the volcanic summits and the giant chasms, the topographic component dominates.

[45] Suppression of noise to achieve physically realistic amplitudes in the inversion need not eliminate the resolution of short-wavelength features. The magnitude of the inver-
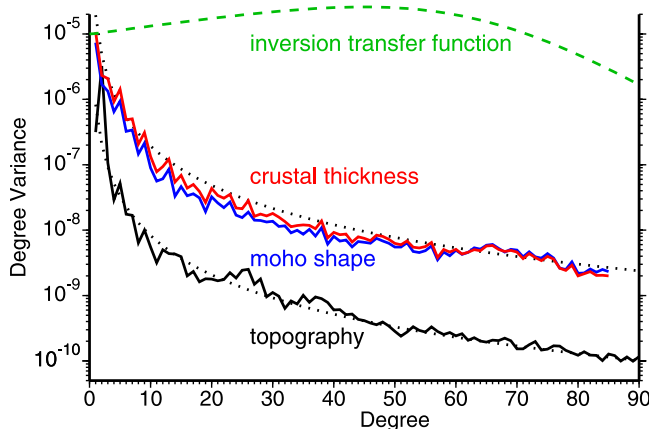
Figure 4. Spectrum of topography versus Moho topography and crustal thickness. The topographic power law of *Smith et al.* [2001b] is shown by dotted lines, offset by the ratio $\rho_C/\Delta\rho$ to fit the Moho shape. The inversion transfer function (dashed curve at top, scaled by 10^{-5}) shows the combined effect of downward continuation and noise reduction versus degree.

sion, or transfer function, applied to U_{RB} is shown by the dashed curve in Figure 4. The degree variance in the inversion for Moho relief relative to U_{RB} is nearly 100% at degree 72, corresponding to spatial wavelengths of 300 km, and is 25% at degree 85, the highest degree in the gravity field. Thus information is incorporated at wavelengths as short as 250 km.

5. Results

[46] The radial difference between the crust-mantle density interface and the surface topography (ftp://ltpftp.gsfc.nasa.gov/projects/tharsis/marscrust2/), is represented by spherical harmonic coefficients to degree 85. The largest single component of the crustal thickness is the degree one zonal, or (1, 0) term, which represents a sinusoidal component of the latitudinal structure, or pole-to-pole slope; this term accounts for more than 80% of the degree 1 variance and for the ~3-km center-of-figure offset to the south relative to the center of mass. The remainder of the degree 1 power, in the (1, 1) terms, represents a substantial thickening of crust in the direction of the Tharsis construct (262.4°E). The degree 2 components, which represent much of the non-hydrostatic character of Tharsis [*Zuber and Smith*, 1997] and its antipode, are an order of magnitude smaller in variance than the degree 1 terms.

5.1. Crustal Thickness Variations

[47] Assuming 600 kg m^{-3} crust-mantle density contrast, our model crustal thickness varies from 5.8–102 km, with the smallest values near the center of Isidis and the northwestern floor of Hellas Planitia. The crustal thickness certainly cannot be less than 0. Our chosen value of 45 km mean crustal thickness results in roughly 6 km of crust at the center of Isidis. Since the relief of Isidis' 5-km-high rim has been largely obliterated in the northeast, and its floor is buried by several km of Syrtis Major flows [*Frey et al.*, 2000], 5 km of crust might result from subsequent infill of the basin interior. The global mean thickness could be as

low as 43.5 km [*Zuber et al.*, 2000], but much thinner crust than assumed in our model seems unlikely. This places a lower bound of 6×10^9 km^3 for the volume of the crust. A similar argument applies to the floor of the 10-km-deep Hellas basin, whose interior has been extensively modified [*Moore and Wilhelms*, 2001] and exhibits <7 km thickness in our model.

[48] The amplitude of crustal variations in our model scales inversely in magnitude with the Moho density contrast $\Delta\rho = 600$ kg m^{-3}. If in our model we had assumed a crustal density of 2700, a similar model with 5 km thickness in Isidis would have required only 35 km mean thickness. A crustal density of 3100 (smaller $\Delta\rho$), on the other hand, requires 65 km mean thickness to match the Bouguer signal and maintain a minimum thickness of 5 km. These extremes are consistent with the value of 50 ± 12 km advocated by *Wieczorek and Zuber* [2004] on the basis of a combination of several geophysical and geochemical studies.

[49] An equal-area histogram of crustal thickness (Figure 5) shows that the global crustal structure is resolved into two major peaks, at approximately 32 km and 58 km. The crustal dichotomy is demarcated by the local minimum in the histogram at 40 km. The heavily cratered highlands contribute the largest peak, with nearly all the crust thicker than 60 km confined to the southern hemisphere. The lowlands peak is broader than that of the uplands, owing to the quasi-sinusoidal character (i.e., degree one zonal component) of the crustal thickness distribution. While the southern highlands have a relatively uniform thickness, the northern lowlands and Arabia Terra region of the southern hemisphere collectively show a latitudinally dependent crustal thickness structure. The crust thickens southward of Lunae Planum and Sinai Planum, contributing to a wide shoulder to the histogram beyond 70 km, with the thickest crust corresponding to the Claritis and Thaumasia structures on the Tharsis rise. Alba Patera, Olympus and Ascraeus Mons are the areas in the north with the thickest crust. The relatively younger northern lowlands comprise the majority of thinner crust, with the Hellas and Argyre Basins contributing the only southern crust that is thinner than 30 km. The
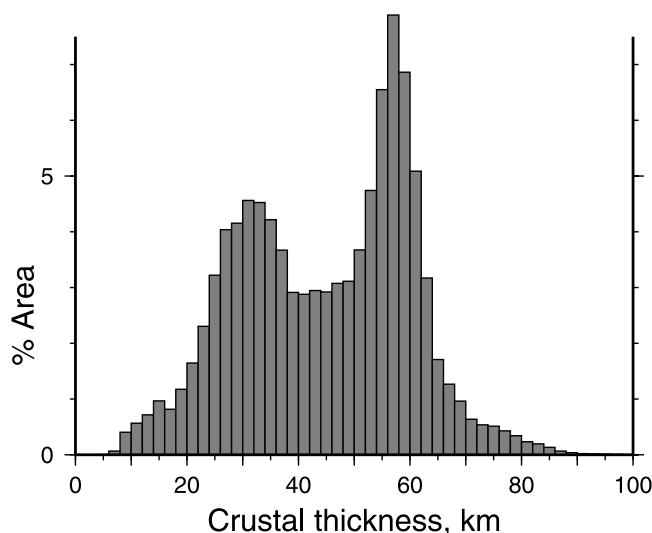

Figure 5. Histogram of crustal thickness, the difference between surface and mantle relief, versus area.
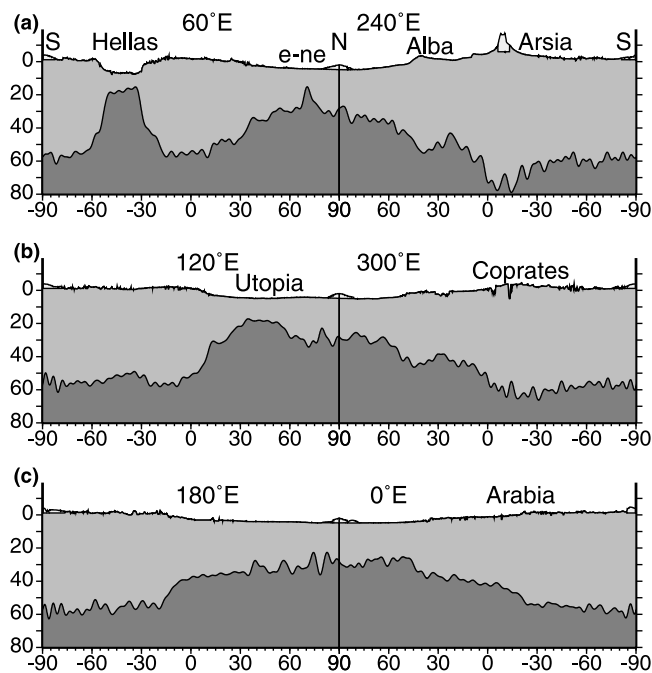
Figure 6. Crustal structure showing the pole-to-pole variations along three longitudinal great circle transects. Regions at the poles and through Arsia Mons that have been modeled with local density anomalies are shown in lighter shades. Vertical exaggeration 60:1.

major impact basins collectively contribute a small histogram peak from 5 to 20 km.

[50] Crustal structure profiles along longitudes (Figure 6) through the dichotomy boundary show thickening beneath the highland and Tharsis provinces and thinning beneath the lowland plains. Transitions in thickness between crustal provinces in eastern Mars are abrupt, corresponding to the relatively steep topographic signature of the dichotomy boundary [*Frey et al.*, 1998] while elsewhere the crust thickens more gradually, in a manner similar to the topographic pole-to-pole slope [*Smith and Zuber*, 1996]. Figure 6c shows that in both the Arabia and Elysium regions the dichotomy boundary is compensated by a crustal thickness variation, with more pronounced relief along the Moho than at the surface. In Arabia, however, the edge of the transition in Moho depth lies northward of the steepest portion of the topographic scarp of the dichotomy boundary. Similarly, the transition in mantle depth beneath Chryse and Acidalia Planitia occurs several degrees eastward of the Lunae Planum and Tempe Terra topographic rises. The associated uncompensated mass deficit produces linear, negative gravity anomalies [cf. *Smith et al.*, 1999a; *Zuber et al.*, 2000; *Phillips et al.*, 2001].

[51] Where the profile at 300°E (Figure 6b) crosses Valles Marineris over a narrow portion of Coprates Chasma, crustal thinning is resolvable at a 300 km wavelength, about 5° of latitude, although the chasm itself is somewhat narrower. The model is only partially resolved, owing to the filters applied to mitigate noise, but crustal thinning is apparently insufficient to compensate the Eos and Coprates deeps, resulting in ~300−500-mGal negative gravity anomalies [*Lemoine et al.*, 2001; *Yuan et al.*, 2001].

[52] Hellas and Utopia show prominent crustal thinning, as with the comparable-sized lunar South Pole-Aitken basin [*Neumann et al.*, 1996; *Wieczorek and Phillips*, 1998]. Hellas' crustal thickness variation is dramatic along the edges of the basin (Figure 6a). The crustal thickness is fairly uniform within 500 km of the center of both Hellas and Utopia (Figures 6a and 6b), increasing at greater distances. In contrast, the crustal thickness increases rapidly within 350 km of the center of Isidis and Argyre.

[53] The Tharsis province consists of greatly thickened crust, consistent with its predominantly volcanic mechanism of formation [*Solomon and Head*, 1981], although Figure 6 shows that the bulk of the Martian crust lies in the southern highlands. The broad Alba Patera rise overlies thickened crust, and the thickest crust of Mars lies below the Arsia Mons volcanic construct in the southern Tharsis Plateau. Tharsis is encompassed by a roughly circular bulge ~6000 km in diameter straddling the equator and covering more than 1/6 of the planet [cf. *Zuber and Smith*, 1997]. This province includes Alba Patera, Tempe Terra, Lunae Planum and the Olympus Mons aureoles in the north, and the Tharsis Montes, Daedalia, Syria, Sinai, Solis, and Icarius Planae in the south. Restricting our consideration to this circular region, the volume of this province is 1.5×10^9 km^3, of which 0.36×10^9 km^3 was required to form the Tharsis rise beyond that of the southern highlands. This volume places an upper bound on the amount of volcanic material emplaced by Tharsis formation [cf. *Phillips et al.*, 2001].

[54] Table 3 gives thicknesses at historical and selected landing sites. It is evident that the regions explored thus far, as well as the Isidis Planitia site targeted by the Beagle Lander, lie within the lowland portion of the dichotomy. The Mars Exploration Rovers landed in moderately thickened crust, while the thickest terrains remain inaccessible to landed probes because of their latitude and inadequate atmospheric density at their higher elevation.

[55] Figure 7 shows the thickness model in map view. The crustal dichotomy boundary, as determined by the 40-km contour, broadly parallels the geologically mapped boundary but places much of the heavily cratered Arabia Terra within the thin crustal province, In contrast, the geologically inferred dichotomy boundary passes north of Arabia and south of the Tharsis Montes. As noted by *Zuber et al.* [2000], Arabia Terra has a crustal thickness representative of the northern lowlands rather than southern highlands. The lowlands crustal province excludes the entire Tharsis region, except small portions of Mareotis Fossae, Kasei Valles and Coprates Chasma. The excursions of thin crust into the Tharsis region have a linear character that suggests tectonic control of these channeled regions [*Anderson and Grimm*, 1998].

Table 3. Selected Model Crustal Thicknesses

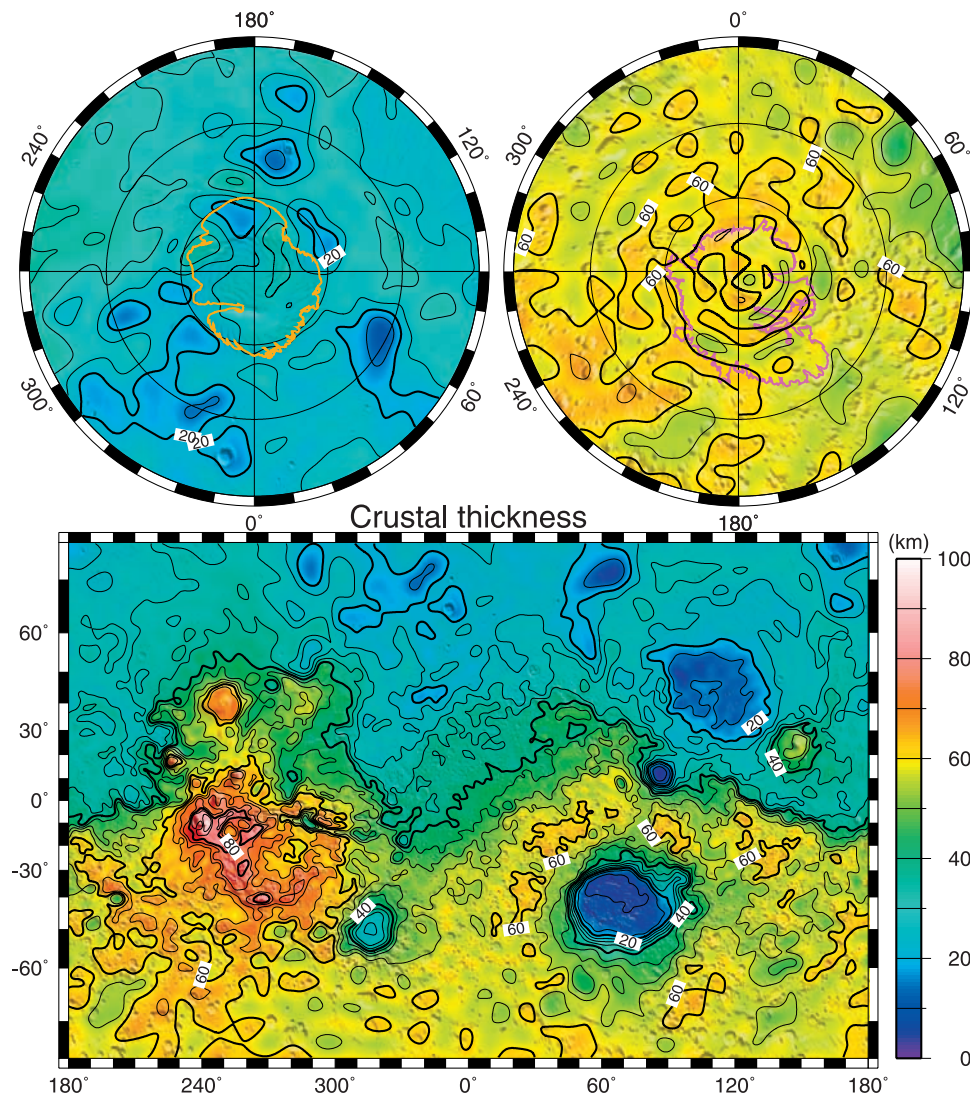| Longitude[a]	Latitude	Elevation	Name	Thickness, km
134.26	47.67	−4500	VL2	21.4
312.032	22.271	−3635	VL1	28.8
326.7	19.55	−3780	Pathfinder	29.8
90.5	11.6	−3770.	Isidis	14.
354.5	−2	−1400	Meridiani	39.2
175.5	−14.5	−1900	Gusev	47.4

[a]Areocentric (IAU2000).

Figure 7. Degree 1-85 crustal thickness model (5 km contours), in Mercator and polar stereographic projections as in Figure 3.

[56] The highland provinces to the south of the 40-km contour comprise roughly five eighths of the surface area, but make up 75% of the volume of the primordial crust. South of 60°S, the cratered highlands exhibit very uniform crustal structure, with a mean of 59 km and standard deviation of 2.9 km. Thinning of crust in the 300-km-diameter Newton and Copernicus basins in the southern highlands stands out against the modest background variations, while an association of thinned crust with some of the larger, more topographically muted basins cannot be confirmed. In spite of its size and preservation, the south polar Prometheus Basin does not exhibit crustal thinning; the annular rings about the pole in our model are likely an artifact of unreliable high-degree zonal potential coefficients.

[57] After correction for the density of polar ices, our model reveals the underlying thin crust common to much of the northern lowlands. The crustal thickness in the lowlands, despite benign topography, varies appreciably more than the relatively uniform highland crust. The greater topographic variance likely reflects modification of the primary lowlands crust by impacts and subsequent volcano-tectonic activity. Crustal anomalies in the vicinity of Korolev and Lomonosov at 290°E, 72°N and 170°E, 75°N are more extensive than the craters themselves, and these anomalies may be older and unrelated to the visible craters. The most prominent anomaly "E−NE" at 63°E, 71°N is thinner than 10 km. This polar anomaly has no topographic or geological expression and is overlain by Hesperian northern plains volcanics and tectonic lineations [*Withers and Neumann*, 2001; *Head et al.*, 2002]. The prevalence of large north polar anomalies suggests that this terrain preserves ancient impacts that predate the visible record.

[58] The crust is thinned beneath nearly all major impact basins and some large craters, as noted in the Bouguer anomaly map. Table 4 gives the minimum model thickness for the four largest basins. The thinned crust beneath Hellas is asymmetric N−S, and its structure is elongated by about 12% in the E−W direction, while others are roughly circular. Modification via volcanic emplacement or crustal flow in a weaker lithosphere to the south might account for such asymmetry, although alternative explanations have been suggested [e.g., *Schultz*, 1997].

Table 4. Basin Minimum Crustal Thickness, Moho Relief, and Superisostatic Uplift in Kilometers

Name	Center[a]		Diameter[b]	Min. Thickness	Relief[c]	Uplift[d]
Utopia	40°N	112°E	4300	9.7	17	5
Hellas	40°S	69°E	3950	6.6	40	0
Isidis	12°N	86.5°E	1950	5.8	36	22
Argyre	51°S	316.5°E	1800	23.7	27	10

[a]Centroid of basin from topography and gravity, which may differ from earlier works owing to geophysical control.
[b]Diameter of annulus of thickened crust surrounding basin, in kilometers.
[c]Radially averaged Moho relief.
[d]Moho height above that required to compensate basin.

[59] Only a few of the highly degraded basins previously inferred from geological mapping [*Schultz et al.*, 1982; *Schultz and Frey*, 1990] express a resolvable geophysical signature. For example, a circular structure in Arcadia [*Schultz et al.*, 1982; *Schultz and Frey*, 1990; *Fuller and Head*, 2002] (190°E30°N) suggests a multiring basin. Many of these previously mapped features are near the resolution of the gravity field. High topographic resolution and inadequate sampling of gravitational power at medium wavelengths can result in spurious features in the crustal thickness model [*Smith and Zuber*, 2002]. Consequently, a crustal thickness anomaly may be indicative of surface topography rather than deeper variations in crustal structure, and caution is needed before ascribing deeper structure such as buried impacts to small anomalies.

5.2. Regional Mantle Depth Variations

[60] Figure 8 shows our preferred model of Moho depth. As a consequence of our correction for the density of the polar ice, the depth to the Moho is relatively constant at each pole, rather than deepening as in the model of *Zuber et al.* [2000]. The depth to mantle increases from the north pole, 38 km below an ellipsoidal datum, to the south, reaching 68 km depth. Since the average depth is assumed, the precise depth to Moho is only constrained in a relative sense; nevertheless, half of the deepening occurs at the hemispheric dichotomy between roughly 10°N/S, while the remainder follows a gradual pole-to-pole slope. The deepest mantle occurs in southern Tharsis near Syria and Solis Planum, and exceeds 80 km depth beneath the Thaumasia rise.

[61] Neither Olympus, Ascraeus, Pavonis Mons nor any of the smaller volcanos exhibit local compensation by deepening of the mantle. Their surface expressions were explicitly modeled as having denser surface composition; otherwise, they would exhibit crustal thinning. Their interiors may indeed be denser than we have assumed.

[62] The broad Arsia, Alba and Elysium volcanic features, or domal rises, are supported mainly by depression of the crust-mantle boundary, and therefore did not require very thick lithospheric or dynamic support, unlike the Olympus Mons edifice [*McGovern et al.*, 2002]. On the basis of surficial distribution of tectonic features, *McGovern et al.* [2001, 2002] suggested that these features were formed via intrusive sills with superposed volcanics.

[63] The shallowest Moho lies beneath Isidis Planitia, closely followed by Hellas, Utopia, "E−NE", and to a lesser extent Argyre and "NWO". The cratering process on the Moon and other planets is thought to remove large quantities of crust, replaced by uplifted mantle [e.g., *Wieczorek and*

Phillips, 1999], and in the case of lunar mascon basins, this mantle uplift is super-isostatic and persists to the present day. Surficial fill by mare also contributes to the positive lunar gravity anomalies, although this fill appears in many cases to have been minimal or absent. The extent to which impact excavation of crust occurs in martian basins and is preserved over geologic time may be quantified by the relief of Moho in our model relative to the deepest immediately surrounding mantle (Table 4). These values are taken from radially averaged profiles of surface and Moho relief, which do not take into account the topographic asymmetries of these basins nor local effects from surrounding volcanos and impacts, but nevertheless reveal appreciable differences in basin relief.

[64] A profile illustrating mantle super-isostatic uplift is shown in Figure 9. If the surface equipotential topography were fully compensated, disregarding possible basin fill of anomalous density, the Moho relief would mirror that of the surface, scaled by the ratio of crustal density to density contrast at the crust-mantle interface, or 2900/600. An example is the Hellas basin, whose Moho relief is very nearly in isostatic equilibrium. The other three basins, most notably Isidis, have varying degrees of super-isostatic loading or Moho uplift.

5.3. Impact Redistribution of Crust

[65] We now contrast the crustal morphologies of the four major basins. The degree of impact modification is greatest in the case of Hellas, whose crust has been displaced outward to form a broad rim [*Zuber et al.*, 2000]. Utopia's rim is most clearly seen in map view as a ring of 10-km thicker crust (Figure 7), overprinted by the Isidis Basin and Elysium Mons. The mantle plugs of Hellas and Utopia are flat-topped (Figure 6). The northeastern Hellas rim appears to form part of the dichotomy boundary, while to the southwest the rim is indistinct and overprinted by the Amphitrites Patera complex. Hellas has a relatively flat floor, sloping somewhat northward, with most of its mantle relief developed toward the margins. Isidis and Argyre have relatively flat floors, but their mantle relief is paraboloidal (Figure 9). The excavation of crust by the impact is concentrated at the center of Isidis and Argyre. In contrast, the mantle relief of Utopia and Hellas develops near the basin walls; relief is modest within 500 km of their centers. Such morphology would result if the mantle was exposed by the impact over a ∼1000-km-wide region, rose isostatically, and was subsequently covered by a few km of crustal material over the basin floor.

[66] Utopia's preserved internal structure reflects the least amount of crustal excavation of the four major basins (Table 4). This basin has been filled by materials associated with the resurfacing of the northern lowlands [*Zuber et al.*, 2000], resulting in the present-day mascon. The crust thickens slightly toward the center, perhaps from the deposition of many km of light, water-deposited sediments [*Thomson and Head*, 2001; *Buczkowski and Cooke*, 2004]. Its surficial rim has been eroded and embayed by the Vastitis Borealis formation north of the depression, while in the south the surrounding surface is covered by Isidis Planitia. However, >10 km of crustal thickening remains at a radius of 2150 km, analogous to features preserved in association with large impact basins on the
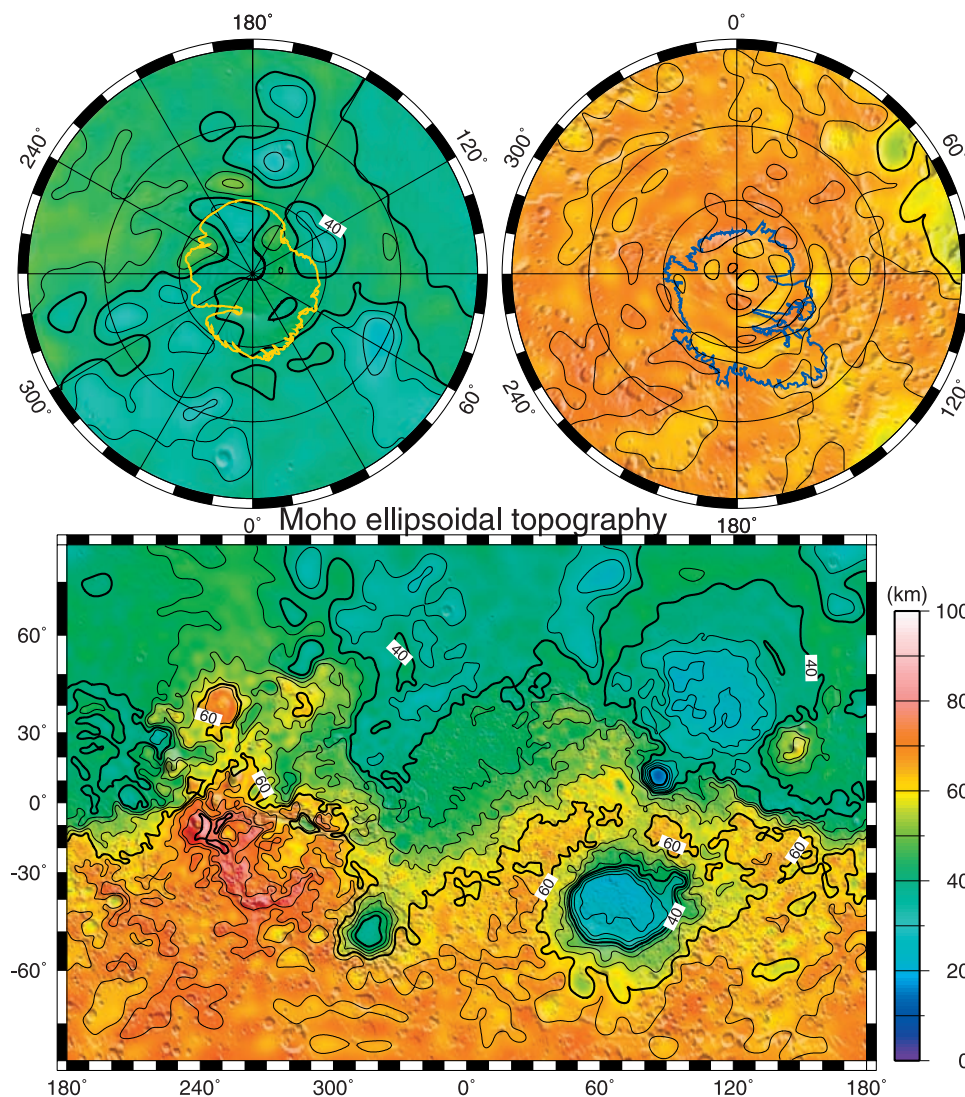
Figure 8. Moho relief (5 km contours), in Mercator and polar stereographic projections as in Figure 3. The degree 2 zonal component is removed. Polar masks of layered terrain show regions where a lower density is applied to compute the residual Bouguer anomaly. Similarly, a higher density is applied within the enclosing contours of the Tharsis volcanoes (not shown).

Moon [*Zuber et al.*, 1994]. If Utopia's annulus of thickened crust is indicative of its size, it is then the largest discernible basin on Mars (but slightly smaller than originally proposed by *McGill* [1989] on the basis of geological mapping). Utopia's moderate Moho relief could have resulted from post-impact viscous flow, but such flow would have removed the steeper mantle relief near the edges of the basin. Modest relief more likely resulted because there was simply less target crust available for redistribution.

[67] The Hellas impact event appears to have redistributed crust radially over nearly the same diameter as Utopia, but the surface and Moho have substantially greater relief. The Hellas crustal rim is diffuse and extends radially over several hundred km. Argyre and Isidis also have diffuse annuli of thickened crust and depressed mantle. Argyre, the smallest of the four basins, has greater relief than Utopia, the largest, as do Hellas and Isidis. This paradox may be explained by the fact that, like Hellas, Argyre is located in thick southern highland crust.

[68] Isidis is positioned at the hemispheric dichotomy boundary, surrounded by thick crust, and is sufficiently close to Hellas and Utopia that the pre-impact crust would have been influenced by the impact events for both of these structures. The Moho relief of Isidis is nearly as great as that of Hellas despite its smaller size.

[69] If one were to attempt to reconstruct the original depth and diameter of excavation from the variations in crustal thickness, as was done for lunar basins by *Wieczorek and Phillips* [1999], the apparent depths of excavation would be less than 50 km. The actual depths might have been substantially greater but would have penetrated the mantle, limiting the amount of crust removed. The inferred diameters of excavation would be a significant fraction of the crustal thickness diameters in Table 4 [*Melosh*, 1989]. Thus it would appear that their transient depth/diameter ratios were considerably less than the 0.1 value obtained by *Wieczorek and Phillips* [1999] for smaller lunar basins up to the size of Orientale or Crisium. The basins in Table 4 more
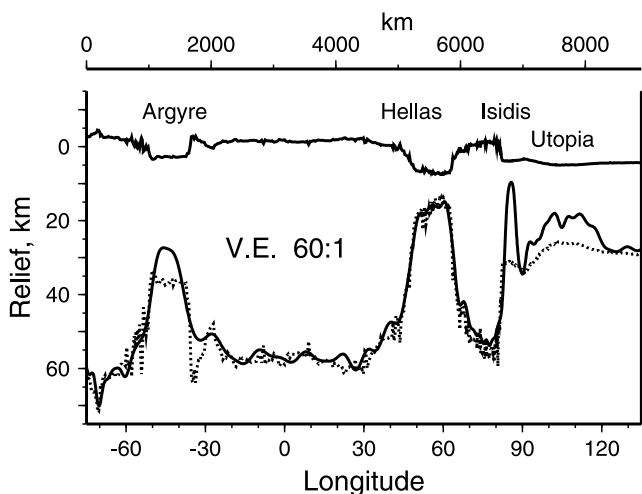
Figure 9. Profiles of surface height and model depth of Moho, relative to an areoid, along a great circle through Tharsis, Argyre, Hellas, Isidis, and Utopia. The mantle relief required to locally compensate the surface topographic load, using our model density contrast, is shown by a dashed curve.

closely resemble the anomalously shallow Serenitatis and Imbrium basins. These basins have undergone varying and diverse surface modification due to erosion, and volcanic and sedimentary infilling. Further structural modeling, as has been done for the Moon [cf. *Wieczorek and Phillips*, 1999], is needed to address the relationship between the current surface expression and subsurface structure of these basins, including estimation of the depth of excavation. Well-resolved comparisons with smaller lunar basins will require refinements in the gravity field of Mars, such as to be provided by the upcoming Mars Reconnaissance Orbiter Mission.

[70] A further measure of impact modification is the degree to which the Moho uplift exceeds that required to compensate present-day surface relief. The Hellas Moho almost exactly mirrors the equipotential topography, scaled by the mantle density contrast, whereas the Isidis, Argyre, and Utopia mantle uplifts overcompensate the basin depressions (Figure 9). Such variations in local isostasy were also found on the Moon, and where ages were known, the Moho relief and amplitude of super-isostatic uplift was inversely correlated with age but not significantly with size [*Neumann et al.*, 1996; *Wieczorek and Phillips*, 1999]. Basins situated in areas on the Moon which were thermally enhanced also tend to be near isostatic equilibrium [*Wieczorek and Phillips*, 2000]. Hellas, like South Pole-Aitken on the Moon, might therefore have impacted a region of thermally enhanced crust, as suggested by lithospheric studies [*Zuber et al.*, 2000; *Nimmo and Stevenson*, 2001; *McGovern et al.*, 2002]. Mars' surface evolution has been long and complex, and detailed modeling of the thermal evolution of its basins may prove fruitful.

5.4. Impact Constraints on Average Crustal Thickness

[71] At 400+ mGal amplitude, the Noachian-age Isidis impact basin forms one of the largest mascon gravity highs in the solar system [*Lemoine et al.*, 2001]. The main

topographic ring is 1500 km in diameter [*Frey et al.*, 2000], and scaling laws [*Melosh*, 1989, equation 5.54] would suggest 60–100 km of excavation. For lunar basins up to half the size of Isidis, like Orientale and Crisium, 26–52 km of crust were removed [*Wieczorek and Phillips*, 1999]. Assuming that nearly all of the pre-Isidis crust was excavated, gravitational restoring forces would produce a central mantle uplift. Such a structure would not result in a mascon, as the gravitational effect of the uplift of denser material balances the mass deficit of the cavity. An additional source of excess mass is required. The present-day gravity anomaly may have resulted from prompt mantle rebound beyond the level required for local isostatic adjustment. Such a phenomenon has been clearly demonstrated on the Moon, where several of the mascon basins appear to have minimal or no infilling by mare basalts [*Konopliv et al.*, 1998]. Whether such prompt super-isostatic rebound could survive in the early Martian thermal environment is uncertain. Alternatively, the basin mascons could result from volcanic or other loading after the crust cooled and the lithosphere thickened [*Comer et al.*, 1985]. We consider an end-member scenario, whereby viscous relaxation occurred following impact, followed by surface loading on a thickened lithosphere, sufficient to produce the present-day plains and to match present-day gravity and topography.

[72] Figure 10 shows such a model. On the left we show the hypothetical state of the crust relatively soon after impact. A transient crater excavates to the depth of the mantle, followed by gravitational rebound. The mantle near the surface is covered by minimal amounts of melt sheets and ejecta fallback. The mass deficit in a central vertical column is in Airy isostatic balance with a deeper, positive mass excess, resulting in a weakly negative gravity anomaly, similar to that seen over Hellas [*Smith et al.*, 1999a].

[73] Modification of the resultant ∼8-km-deep basin continued long after the period of heavy bombardment. Bolides undoubtedly produced many 100-km-diameter
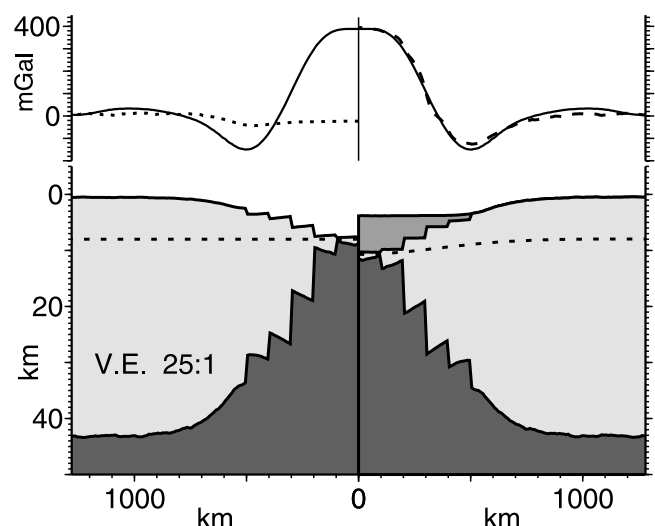

Figure 10. Radially averaged model of Isidis equipotential topography, Moho, and gravity before (left, dots) and after (dashes) surface loading and flexure of a 150-km-thick elastic lithosphere.

craters on this surface, as seen on the basin rim, but such large craters are completely buried by volcanic flows and by mass wasting of the Isidis rim to the northeast. The relicts of such craters seen as quasi-circular depressions in much of the lowlands are also absent [*Frey et al.*, 2002]. The amount of material transferred to the basin interior was evidently substantial.

[74] The Isidis gravity high is surrounded by a ring of negative anomaly that suggests flexure due to a central load and/or thickening of the crust surrounding the impact [*Neumann et al.*, 1996; *Wieczorek and Phillips*, 1999]. Using flexural graben (Nili and Amenthes Fossae), *Comer et al.* [1985] inferred an effective elastic thickness $T_e >$ 125 km. The right side of Figure 10 shows a model where the mantle lithosphere has deformed under a set of concentric cylindrical loads, producing the present-day topographic surface; the flexure due to this load was used to calculate the initial surface topography and isostatic Moho relief shown on the left. We employ the approximations of *Comer et al.* [1985], whereby several cylindrical loads from $100-500$ km radius are superposed to calculate flexure of a thin elastic shell, accounting for fiber and membrane stress, with Young's modulus $E = 1 \times 10^{11}$ Pa and Poisson's ratio $v =$ 0.25 [*Johnson et al.*, 2000]. We use the finite-amplitude Cartesian formulation of *Parker* [1972] to calculate gravity, an adequate approximation given the large uncertainties in model thickness and density.

[75] Volcanic loading by a 3200 kg m^{-3} density basalt, 6.5 km thick, results in 2.7 km flexure at a time when lithosphere has thickened to 150 km. The resulting structure, shown on the right of Figure 10, conforms to the present-day topography and closely matches the radially averaged gravity. In this model, the impact excavated nearly all of the crust at the impact center. This example requires a significant high-density surface load, equivalent to 2.1×10^6 km^3 of basaltic fill, to reproduce the present-day mascon, but does not require super-isostatic mantle uplift. Similar modification of Utopia and Argyre by lesser thicknesses of fill could produce residual mascon anomalies with the shallow Moho depths listed in Table 4.

[76] The 45-km average crustal thickness assumed provides a plausible model for the Isidis mascon. A thinner crust would require super-isostatic uplift and/or unusually high mantle density to explain the post-impact crustal structure, while a thicker global crust would require a substantially greater volcanic load and a cooler geotherm (thicker lithosphere) to resist flexural relaxation and achieve the same mascon amplitude. We do not consider models incorporating a layered crust that, albeit more realistic, would require nearly the same amount of crustal excavation and only introduce more parameters.

6. Discussion

[77] In the absence of strong evidence to the contrary, we have assumed a uniform crustal density and obtain a contrast in thickness between 32 km in the north and 58 km in the south. While a Pratt-like model for the Martian crust could be invoked, as was once considered for the Moon [*Solomon*, 1978], a nearly twofold difference in density contrast would be required to explain the crustal dichotomy, or bulk densities varying from 2700 to 3100 kg m^{-3} south to north. However the Thermal Emission Spectrometer data [*Bandfield et al.*, 2000; *Bandfield*, 2002] suggest a more basaltic composition for dark regions in the south and a more silicic northern composition (but see also *Wyatt and McSween* [2002]), raising the possibility that, if anything, the southern crust might be denser.

[78] Models with lower average crustal density have been proposed. Although *McKenzie et al.* [2002] showed that low crustal densities are consistent with top-loaded admittance models in the Valles Marineris region, the lava-flow origin for layering in the walls of Valles Marineris [*McEwen et al.*, 1999], and the generally competent nature of these formations precludes such a low-density crust in this region. *McGovern et al.* [2002] found that such admittances are equally consistent with a model that incorporates bottom loading in Valles Marineris and employs densities of 2900 kg m^{-3}. Our model predicts bottom loading by up to 10 km of uplifted mantle beneath Coprates and Candor Chasmae. While the extension that gave rise to these valleys may have different origins, shallowing of Moho is consistent with seismic results in narrow terrestrial rift zones [*Buck*, 1991].

[79] Apart from the giant impacts, the highland and lowland crustal thickness anomalies do not correlate significantly with magnetic anomalies [*Connerney et al.*, 1999; *Purucker et al.*, 2000]. While there are small thickness variations in Terra Cimmeria, they are nowhere near as pronounced as the strong magnetic sources at the resolution afforded by the latest data. Any relation between the actual topography or model crustal structure and the magnetization falls short of a simple tectonic characterization (but see *Johnson and Phillips* [2003]).

[80] Our model shows that Mars' crust is, to first order, characterized by a degree 1 structure that is several times larger than any higher degree harmonic component. The Tharsis rise and Hellas annulus represent the strongest components in the degree 2 crustal thickness structure. Any model of planetary evolution must account for the dominance of the dichotomy over the smaller, yet geologically as significant Tharsis bulge.

[81] A simple pole-to-pole slope, i.e., degree 1 offset between the center of figure and center of mass, would produce a uniform distribution of thickness between two extremes. The crustal structure clearly has a bimodal distribution, together with a degree-1 component. The presence of a 58-km crustal thickness peak (Figure 5) suggests a single mechanism for highland crustal formation, with modification by the Hellas impact, followed by additional construction of Tharsis. Such a mechanism would have operated during an early period of high mantle temperature and melt production [*Hauck and Phillips*, 2002]. Such thick crust would have been highly ductile and tended toward uniform thickness, while resisting subduction driven by mantle convection. The Martian crustal dichotomy is more pronounced than that of the Moon, where there is only a single peak in crustal thickness, and where the thickest crust appears to arise from redistribution by the South Pole-Aitken impact [*Zuber et al.*, 1994].

[82] Despite the significant variation of crustal thickness in the northern hemisphere, likely the result of ancient impacts, Hesperian resurfacing has effectively obliterated any surficial expression of these anomalies. Conceivably studies of com-

pletely buried craters could be used to estimate a volume of the northern hemisphere resurfacing [*Frey et al.*, 2002; *Buczkowski and McGill*, 2003], but such estimates cannot be derived from the currently resolved gravity field.

[83] The spatial distribution of the 32-km peak in the northern lowlands crustal thickness distribution is most simply explained by an endogenic mechanism of formation, arguably an early episode of crustal spreading [*Sleep*, 1994; *Nimmo and Stevenson*, 2000; *Zuber*, 2001] or a degree 1 style of mantle convection [*Zhong and Zuber*, 2001]. The largest surviving impact (Utopia) appears to have postdated the formation of the lowland crust. Utopia's variations of crustal thickness are largely preserved, making it unlikely that the northern crust was originally thick, and subsequently thinned by internal processes following the impact [cf. *McGill and Dimitriou*, 2001]. Lacking any new evidence of an impact signature that explains the dichotomy boundary, this study supports the conclusions of *Zuber et al.* [2000] that an exogenic origin for the lowland crust [e.g., *Wilhelms and Squyres*, 1984; *Frey and Schultz*, 1988] is unlikely.

[84] The next largest surviving impact, Hellas, also postdates the formation of the highland crust. Together with Utopia and the putative northern mascon impacts, these observations place a constraint on the timing of the formation of the dichotomy. Differentiation of the two crustal provinces must have been nearly complete prior to the cessation of heavy impacts.

[85] The crustal structure reveals the extent to which the dichotomy has been modified since formation. The dichotomy formed in early Martian history during a time of elevated mantle temperature. Erosional modification of the surficial expression of the boundary [e.g., *Hynek and Phillips*, 2001; *Craddock and Howard*, 2002] possibly occurred after the crust had cooled significantly and was able to support elastic stresses. Flanking Chryse and Acidalia Planitia, the Arabia and Tempe Terra highland terrain may have undergone this later modification, leaving a net mass deficit at the boundary. This deficit is manifest as linear negative gravity anomalies that straddle the highland-lowland boundary and are preserved as troughs seen in the present day gravity field [e.g., *Smith et al.*, 1999a; *Dombard et al.*, 2004]. The work of *Dombard et al.* [2004] argues that wavelength-dependent, partial compensation of the boundary scarp accounts, in large degree, for the gravity troughs, but notes that other factors may explain offsets between synthetic and observed gravity anomalies. By comparing the offset in topographic boundary and compensating mantle root in Arabia and the northeastern edge of Tharsis, we estimate that as much as 2 km of mass wasting occurred along the steepest slopes of the dichotomy, leaving a considerably less distinct boundary scarp overlying the gravity low. The gravity troughs are less apparent along the dichotomy boundary eastward of Arabia, where the topographic boundary is more distinct.

[86] Preservation of the Argyre, Isidis, and Utopia mascons, with the large Moho relief associated with Hellas, indicates early planet-wide cooling of crust [*McGovern et al.*, 2002]. If the Utopia and Hellas events are distinguished mainly by the differing thickness of target crust, then the hemispheric dichotomy in crustal thickness would have predated the formation of the two largest basins. The numerous positive mass anomalies in the flat northern basin preserved in the lowest part of a now-buried crustal sequence are, like the almost obliterated Arcadia feature, probably relicts of an earlier impact history, now virtually erased from the geological record. That remnants of such structures survive and postdate the crustal dichotomy suggests that it existed in something near to its present form during the latter stages of formation of primordial crust and heavy bombardment.

7. Conclusions

[87] Refined gravity and topography from the MGS mission have revealed the crustal structure of Mars to wavelengths approaching 300 km. A terrain-corrected gravity field reveals significant density anomalies associated with the largest volcanos and with the polar caps. Interpretation of the Bouguer anomaly in terms of a single-layered crust of 45-km global mean thickness, while non-unique, is consistent with the geological and thermal history of Mars, while crust thicker than 65 km or thinner than 35 km requires special assumptions regarding the composition and distribution of the crust, particularly at the sites of large impacts. This crustal model reveals two distinct crustal provinces with relatively constant thickness, a distinction preserved since the formation of a crustal dichotomy in the earliest Martian history. These provinces have since been modified by four major visible impacts, by volcanic construction, by tectonic deformation, by large-scale erosion of the boundary, and by possibly several major impacts hidden beneath the northern lowland plains. Impact redistribution of crust appears to have been most pronounced (or at least appears best preserved) in the thicker southern highlands. The greater thickness of highland crust surrounding the Argyre, Hellas and Isidis impacts appears to have allowed greater excavation of crust than Utopia, likely contributing to their greater relief. Better understanding of the differences in density and structure of the crust awaits in situ exploration, particularly of the heretofore inaccessible highland terrain.

References

Anderson, S., and R. E. Grimm (1998), Rift processes at the Valles Marineris: Constraints from gravity on necking and rate-dependent strength evolution, *J. Geophys. Res.*, *103*, 11,113–11,124.

Arkani-Hamed, J. (2000), Strength of Martian lithosphere beneath large volcanoes, *J. Geophys. Res.*, *105*(E11), 26,713–26,732.

Arkani-Hamed, J., and L. Riendler (2002), Stress differences in the Martian lithosphere: Constraints on the thermal state of Mars, *J. Geophys. Res.*, *107*(E12), 5119, doi:10.1029/2002JE001851.

Balmino, G., B. Moynot, and N. Vales (1982), Gravity field of Mars in spherical harmonics up to degree and order eighteen, *J. Geophys. Res.*, *87*, 9735–9746.

Bandfield, J. L. (2002), Global mineral distributions on Mars, *J. Geophys. Res.*, *107*(E6), 5042, doi:10.1029/2001JE001510.

Bandfield, J. L., V. Hamilton, and P. R. Christensen (2000), A global view of Martian surface composition from MGS-TES, *Science*, *287*, 1626–1630.

Bills, B. G., and A. J. Ferrari (1978), Mars topography harmonics and geophysical implications, *J. Geophys. Res.*, *83*, 3497–3508.

Bills, B. G., and M. Kobrick (1985), Venus topography: A harmonic analysis, *J. Geophys. Res.*, *90*, 827–836.

Britt, D. T., and G. J. Consolmagno (2003), Stony meteorite porosities and densities: A review of the data through 2001, *Meteorit. Planet. Sci.*, *38*, 1161–1180.

Brückner, J., G. Dreibus, R. Rieder, and H. Wänke (2003), Refined data of Alpha Proton X-ray Spectrometer analyses of soils and rocks at the Mars Pathfinder site: Implications for surface chemistry, *J. Geophys. Res.*, *108*(E12), 8094, doi:10.1029/2003JE002060.

Buck, W. R. (1991), Modes of continental lithospheric extension, *J. Geophys. Res.*, *96*, 20,161–20,178.

Buczkowski, D. L., and M. L. Cooke (2004), Formation of double-ring circular grabens due to volumetric compaction over buried impact craters: Implications for thickness and nature of cover material in Utopia Planitia, *Mars, J. Geophys. Res.*, *109*(E2), E02006, doi:10.1029/2003JE002144.

Buczkowski, D. L., and G. E. McGill (2003), Utopia Planitia: Observations and models favoring thick water-deposited sediments, in *Sixth International Conference on Mars* [CD-ROM], abstract 3031, Lunar and Planet. Inst., Houston, Tex.

Carr, M. H. (1981), *The Surface of Mars*, Yale Univ. Press, New Haven, Conn.

Comer, R. P., S. C. Solomon, and J. W. Head (1985), Mars: Thickness of the lithosphere from the tectonic response to volcanic loads, *Rev. Geophys.*, *23*, 61–72.

Connerney, J. E. P., et al. (1999), Magnetic lineations in the ancient crust of Mars, *Science*, *284*, 794–798.

Consolmagno, G. J., and M. Strait (2002), The density and porosity of Martian meteorites, *Geol. Soc. Am. Abstr. Programs*, *32-4*.

Craddock, R. A., and A. D. Howard (2002), The case for rainfall on a warm, wet early Mars, *J. Geophys. Res.*, *107*(E11), 5111, doi:10.1029/2001JE001505.

Craddock, R. A., R. Greeley, and P. R. Christensen (1990), Evidence for an ancient impact basin in Daedalia Planum, *Mars, J. Geophys. Res.*, *95*, 10,729–10,741.

Defraigne, P., V. Dehant, and T. V. Hoolst (2001), Steady-state convection in Mars' mantle, *Planet. Space Sci.*, *49*, 501–509.

Dombard, A. J., M. L. Searls, and R. J. Phillips (2004), An alternative explanation for the "buried channels" on Mars: The gravity signal from a sharp boundary on partially compensated, long-wavelength topography, *Geophys. Res. Lett.*, *31*(5), L05701, doi:10.1029/2003GL019162.

Esposito, P. B., W. B. Banerdt, G. F. Lindal, W. L. Sjogren, M. A. Slade, B. G. Bills, D. E. Smith, and G. Balmino (1992), Gravity and topography, in *Mars*, edited by H. H. Kieffer et al., pp. 209–248, Univ. of Ariz. Press, Tucson.

Fishbaugh, K. E., and J. W. Head (2000), North polar region of Mars: Topography of circumpolar deposits from Mars Orbiter Laser Altimeter (MOLA) data and evidence for asymmetric retreat of the polar cap, *J. Geophys. Res.*, *105*, 22,455–22,486.

Fishbaugh, K. E., and J. W. Head (2001), Comparison of the north and south polar caps of Mars: New observations from MOLA data and discussion of some outstanding questions, *Icarus*, *154*(1), 145–161.

Folkner, W. M., C. F. Yoder, D. N. Yuan, E. M. Standish, and R. A. Preston (1997), Interior structure and seasonal mass redistribution of Mars from radio tracking of Mars Pathfinder, *Science*, *178*, 1749–1751.

Forsyth, D. W. (1985), Subsurface loading and estimates of the flexural rigidity of continental lithosphere, *J. Geophys. Res.*, *90*, 12,623–12,632.

Frey, H. V. (2003), Large diameter visible and buried basins on Mars: Implications for age of the highlands and (buried) lowlands and turn-off of the global magnetic field, *Lunar Planet. Sci.*, *XXXIV*, abstract 1838.

Frey, H. V., and R. A. Schultz (1988), Large impact basins and the mega-impact origin for the crustal dichotomy on Mars, *Geophys. Res. Lett.*, *15*, 229–232.

Frey, H. V., B. G. Bills, R. S. Nerem, and J. H. Roark (1996), The isostatic state of Martian topography—Revisited, *Geophys. Res. Lett.*, *23*, 721–724.

Frey, H., S. E. Sakimoto, and J. H. Roark (1998), The MOLA topographic signature of the crustal dichotomy boundary zone on Mars, *Geophys. Res. Lett.*, *25*, 4409–4412.

Frey, H., J. H. Roark, and S. E. H. Sakimoto (2000), Detailed topographic structure of the Isidis impact basin from MOLA data, *Lunar Planet. Sci.*, *XXXI*, abstract 1748.

Frey, H. V., J. H. Roark, K. M. Shockey, E. L. Frey, and S. E. H. Sakimoto (2002), Ancient lowlands on Mars, *Geophys. Res. Lett.*, *29*(10), 1384, doi:10.1029/2001GL013832.

Fuller, E. R., and J. W. Head (2002), Amazonis Planitia: The role of geologically recent volcanism and sedimentation in the formation of the smoothest plains on Mars, *J. Geophys. Res.*, *107*(E10), 5081, doi:10.1029/2002JE001842.

Harder, H., and U. Christensen (1996), A one-plume model of Martian mantle convection, *Nature*, *380*, 507–509.

Hauck, S. A., II, and R. J. Phillips (2002), Thermal and crustal evolution of Mars, *J. Geophys. Res.*, *107*(E7), 5052, doi:10.1029/2001JE001801.

Head, J. W., and S. Pratt (2001), Extensive Hesperian-aged south polar ice sheet on Mars: Evidence for massive melting and retreat, and lateral flow and ponding of meltwater, *J. Geophys. Res.*, *106*, 12,275–12,299.

Head, J. W., III, M. A. Kreslavsky, and S. Pratt (2002), Northern lowlands of Mars: Evidence for widespread volcanic flooding and tectonic deformation in the Hesperian Period, *J. Geophys. Res.*, *107*(E1), 5003, doi:10.1029/2000JE001445.

Hynek, B., and R. J. Phillips (2001), Evidence for extensive denudation of the Martian highlands, *Geology*, *29*(5), doi:10.1130/0091-7613, 407–410.

Johnson, C. L., and R. J. Phillips (2003), The Tharsis region of Mars: New insights from magnetic field observations, in *Sixth International Conference on Mars* [CD-ROM], abstract 3065, Lunar and Planet. Inst., Houston, Tex.

Johnson, C. L., S. C. Solomon, J. W. Head, R. J. Phillips, D. E. Smith, and M. T. Zuber (2000), Lithospheric loading by the north polar cap of Mars, *Icarus*, *144*, 313–328.

Kaula, W. M. (1966), *Theory of Satellite Geodesy*, Blaisdell, Waltham, Mass.

Kiefer, W. S. (2004), Gravity evidence for an extinct magma chamber beneath Syrtis Major, Mars: A look at the magmatic plumbing system, *Earth Planet. Sci. Lett.*, *222*, 349–361.

Kiefer, W. S., B. G. Bills, and R. S. Nerem (1996), An inversion of gravity and topography for mantle and crustal structure on Mars, *J. Geophys. Res.*, *101*, 9239–9252.

Kieffer, H. H., and A. P. Zent (1992), Quasi-periodic climate change on Mars, in *Mars*, edited by H. H. Kieffer et al., pp. 1180–1218, Univ. of Ariz. Press, Tucson.

Konopliv, A. S., and W. L. Sjogren (1995), The JPL Mars gravity field, Mars50c, based upon Viking and Mariner 9 Doppler tracking data, *JPL Publ. 95-5*, 73 pp., Jet Propul. Lab., Pasadena, Calif.

Konopliv, A. S., A. Binder, L. Hood, A. Kucinskas, W. L. Sjogren, and J. G. Williams (1998), Gravity field of the Moon from Lunar Prospector, *Science*, *281*, 1476–1480.

Lemoine, F. G., D. E. Smith, D. D. Rowlands, M. T. Zuber, G. A. Neumann, D. S. Chinn, and D. E. Pavlis (2001), An improved solution of the gravity field of Mars (GMM-2B) from Mars Global Surveyor, *J. Geophys. Res.*, *106*, 23,359–23,376.

McEwen, A. S., M. C. Malin, M. H. Carr, and W. K. Hartmann (1999), Voluminous volcanism on early Mars revealed in Valles Marineris, *Nature*, *397*, 584–586.

McGill, G. E. (1989), Buried topography of Utopia, Mars: Persistence of a giant impact depression, *J. Geophys. Res.*, *94*, 2753–2759.

McGill, G. E., and A. M. Dimitriou (2001), The Utopia Basin revisited: Regional slope and shorelines from MOLA profiles, *Geophys. Res. Lett.*, *28*, 411–414.

McGovern, P. J. (2002), Interpretations of gravity anomalies at Olympus Mons, Mars: Intrusions, impact basins, and troughs, *Lunar Planet. Sci.*, *XXXIII*, abstract 2024.

McGovern, P. J., S. C. Solomon, J. W. Head, D. E. Smith, M. T. Zuber, and G. A. Neumann (2001), Extension and uplift at Alba Patera: Insights from MOLA observations and loading models, *J. Geophys. Res.*, *106*, 23,769–23,809.

McGovern, P. J., S. C. Solomon, D. E. Smith, M. T. Zuber, M. Simons, M. A. Wieczorek, R. J. Phillips, G. A. Neumann, O. Aharonson, and J. W. Head (2002), Localized gravity/topography admittance and correlation spectra on Mars: Implications for regional and global evolution, *J. Geophys. Res.*, *107*(E12), 5136, doi:10.1029/2002JE001854.

McGovern, P. J., et al. (2004), Correction to "Localized gravity/topography admittance and correlation spectra on Mars: Implications for regional and global evolution," *J. Geophys. Res.*, *109*, E07007, doi:10.1029/2004JE002286.

McKenzie, D., D. N. Barnett, and D. Yuan (2002), The relationship between Martian gravity and topography, *Earth Planet. Sci. Lett.*, *195*, 1–16.

McSween, H. Y. (1985), SNC meteorites: Clues to Martian petrologic evolution?, *Rev. Geophys.*, *23*, 391–416.

McSween, H. Y. (1994), What we have learned about Mars from SNC meteorites, *Meteoritics*, *29*, 757–779.

Melosh, H. J. (1989), *Impact Cratering: A Geologic Process*, Oxford Univ. Press, New York.

Moore, J. M., and D. E. Wilhelms (2001), Hellas as a possible site of ancient ice-covered lakes on Mars, *Icarus*, *154*, 258–276.

Mutch, T. A., R. E. Arvidson, J. W. Head, K. L. Jones, and R. S. Saunders (1976), *The Geology of Mars*, Princeton Univ. Press, Princeton, N. J.

Neumann, G. A., M. T. Zuber, D. E. Smith, and F. G. Lemoine (1996), The lunar crust: Global structure and signature of major basins, *J. Geophys. Res.*, *101*, 16,841–16,863.

Neumann, G. A., D. D. Rowlands, F. G. Lemoine, D. E. Smith, and M. T. Zuber (2001), Crossover analysis of Mars Orbiter Laser Altimeter data, *J. Geophys. Res.*, *106*, 23,753–23,768.

Nimmo, F. (2002), Admittance estimates of mean crustal thickness and density at the Martian hemispheric dichotomy, *J. Geophys. Res.*, *107*(E11), 5117, doi:10.1029/2000JE001488.

Nimmo, F., and D. J. Stevenson (2000), The influence of early plate tectonics on the thermal evolution and magnetic field of Mars, *J. Geophys. Res.*, *105*, 11,969–11,980.

Nimmo, F., and D. J. Stevenson (2001), Estimates of Martian crustal thickness from viscous relaxation of topography, *J. Geophys. Res.*, *106*, 5085–5098.

Norman, N. D. (1999), The composition and thickness of the crust of Mars estimated from rare earth elements and neodymium-isotopic composition of Martian meteorites, *Meteorit. Planet. Sci.*, *34*, 439–449.

Oppenheim, A. V., and R. W. Schafer (1975), *Digital Signal Processing*, Prentice-Hall, Old Tappan, N. J.

Parker, R. L. (1972), The rapid calculation of potential anomalies, *Geophys. J. R. Astron. Soc.*, *31*, 447–455.

Phillips, R. J. (1988), The geophysical signal of the Martian global dichotomy, *Eos Trans. AGU*, *69*(16), 389.

Phillips, R. J., R. S. Saunders, and J. E. Conel (1973), Mars: Crustal structure inferred from Bouguer anomalies, *J. Geophys. Res.*, *78*, 4815–4820.

Phillips, R. J., et al. (2001), Ancient geodynamics and global-scale hydrology on Mars, *Science*, *291*, 2587–2591.

Phipps Morgan, J., and D. K. Blackman (1993), Inversion of combined gravity and bathymetry data for crustal structure: A prescription for downward continuation, *Earth Planet. Sci. Lett.*, *119*, 167–179.

Priestley, T. I., A. K. Baird, B. C. Clark, K. Keil, H. J. Rose, R. P. Christian, P. H. Evans, and W. C. Kelliher (1977), Geochemical and mineralogical interpretation of the Viking inorganic chemical results, *J. Geophys. Res.*, *82*, 4625–4634.

Purucker, M., D. Ravat, H. Frey, C. Voorhies, T. Sabaka, and M. Acuna (2000), An altitude normalized magnetic map of Mars and its interpretation, *Geophys. Res. Lett.*, *27*, 2449–2452.

Rieder, R., T. Economou, H. Wanke, A. Turkevich, J. Crisp, J. Breckner, G. Dreibus, and H. Y. McSween (1997), The chemical composition of Martian soil and rocks returned by the mobile alpha proton X-ray spectrometer: Preliminary results from the X-ray mode, *Science*, *278*, 1771–1774.

Schultz, P. H. (1997), Forming the South-pole Aitken Basin: The extreme games, *Lunar Planet. Sci.*, *XXVIII*, abstract 1787.

Schultz, P. H., R. A. Schultz, and J. Rogers (1982), The structure and evolution of ancient impact basins on Mars, *J. Geophys. Res.*, *87*, 9803–9820.

Schultz, R. A., and H. V. Frey (1990), A new survey of multiring basins on Mars, *J. Geophys. Res.*, *95*, 14,175–14,189.

Seidelmann, P. K., et al. (2002), Report of the IAU/IAG working group on cartographic coordinates and rotational elements of the planets and satellites: 2000, *Cel. Mech. Dyn. Astron.*, *82*, 83–110.

Sleep, N. H. (1994), Martian plate tectonics, *J. Geophys. Res.*, *99*, 5639–5655.

Smith, D. E., and M. T. Zuber (1996), The shape of Mars and the topographic signature of the hemispheric dichotomy, *Science*, *271*, 184–188.

Smith, D. E., and M. T. Zuber (2002), The crustal thickness of Mars: Accuracy and resolution, *Lunar Planet. Sci.*, *XXXIII*, abstract 1893.

Smith, D. E., F. J. Lerch, R. S. Nerem, M. T. Zuber, G. B. Patel, S. K. Fricke, and F. G. Lemoine (1993), An improved gravity model for Mars: Goddard Mars Model-1 (GMM-1), *J. Geophys. Res.*, *98*, 20,781–20,889.

Smith, D. E., W. L. Sjogren, G. L. Tyler, G. Balmino, F. G. Lemoine, and A. S. Konopliv (1999a), The gravity field of Mars: Results from Mars Global Surveyor, *Science*, *286*, 94–96.

Smith, D. E., et al. (1999b), The global topography of Mars and implications for surface evolution, *Science*, *284*, 1495–1503.

Smith, D. E., M. T. Zuber, and G. A. Neumann (2001a), Seasonal variations of snow depth on Mars, *Science*, *294*, 2141–2146.

Smith, D. E., et al. (2001b), Mars Orbiter Laser Altimeter: Experiment summary after the first year of global mapping of Mars, *J. Geophys. Res.*, *106*, 23,689–23,722.

Smith, D. E., G. A. Neumann, R. E. Arvidson, E. A. Guinness, and S. Slavney (2003), Mars Orbiter Laser Altimeter Mission Experiment Gridded Data Record, *MGS–M-MOLA–5-MEGDR–L3-V1.0*, NASA Planet. Data Syst., Washington, D. C.

Sohl, F., and T. Spohn (1997), The interior structure of Mars: Implications from SNC meteorites, *J. Geophys. Res.*, *102*, 1613–1635.

Solomon, S. C. (1978), The nature of isostasy on the Moon: How big a Pratt-fall for Airy models?, *Proc. Lunar Planet. Sci. Conf. 9th*, 3499–3511.

Solomon, S. C., and J. W. Head (1981), Evolution of the Tharsis province of Mars: The importance of heterogeneous lithospheric thickness and volcanic construction, *J. Geophys. Res.*, *82*, 9755–9774.

Thomson, B. J., and J. W. Head (2001), Utopia Basin, Mars: Characterization of topography and morphology and assessment of the origin and evolution of basin internal structure, *J. Geophys. Res.*, *106*(E10), 23,209–23,230.

Touma, J., and J. Wisdom (1993), The chaotic obliquity of Mars, *Science*, *259*, 1294–1297.

Turcotte, D. L., R. Scherbakov, B. D. Malamud, and A. B. Kucinskas (2002), Is the Martian crust also the Martian elastic lithosphere?, *J. Geophys. Res.*, *107*(E11), 5091, doi:10.1029/2001JE001594.

Tyler, G. L., et al. (2002), JGM85H02.SHA, in *MGS RST Science Data Products, USA_NASA_JPL_MORS_1019*, edited by R. A. Simpson, *MGS–M–RSS–5–SDP–V1.0*, NASA Planet. Data Syst., Washington, D. C.

Tyler, G. L., et al. (2003), GGM1041C.SHA, in *MGS RST Science Data Products, USA_NASA_JPL_MORS_1021*, edited by R. A. Simpson, *MGS–M–RSS–5–SDP–V1.0*, NASA Planet. Data Syst., Washington, D. C.

Tyler, G. L., et al. (2004), JGM95I01.SHA, in *MGS RST Science Data Products, USA_NASA_JPL_MORS_1024*, edited by R. A. Simpson, *MGS–M–RSS–5–SDP–V1.0*, NASA Planet. Data Syst., Washington, D. C.

Vening Meinesz, F. A. (1950), A remarkable feature of the Earth's topography, *Proc. K. Ned. Akad. Wet.*, *53*(7), 973–974.

Wieczorek, M. A., and R. J. Phillips (1998), Potential anomalies on a sphere: Applications to the thickness of the lunar crust, *J. Geophys. Res.*, *103*, 1715–1724.

Wieczorek, M. A., and R. J. Phillips (1999), Lunar multiring basins and the cratering process, *Icarus*, *139*, 246–259.

Wieczorek, M. A., and R. J. Phillips (2000), The "Procellarum KREEP Terrane": Implications for mare volcanism and lunar evolution, *J. Geophys. Res.*, *105*, 20,417–20,430.

Wieczorek, M. A., and M. T. Zuber (2004), The thickness of the Martian crust: Improved constraints from geoid-to-topography ratios, *J. Geophys. Res.*, *109*(E1), E01009, doi:10.1029/2003JE002153.

Wilhelms, D. E., and S. W. Squyres (1984), The Martian hemispheric dichotomy may be due to a giant impact, *Nature*, *309*, 138–140.

Withers, P., and G. A. Neumann (2001), Enigmatic northern plains of Mars, *Nature*, *410*, 651.

Wyatt, M. B., and H. Y. J. McSween (2002), Spectral evidence for weathered basalt as an alternative to andesite in the northern lowlands of Mars, *Nature*, *417*, 263–266.

Yoder, C. F., A. S. Konopliv, D. N. Yuan, E. M. Standish, and W. M. Folkner (2003), Fluid core size of Mars from detection of the solar tide, *Science*, *300*, 299–303.

Yuan, D. N., W. L. Sjogren, A. S. Konopliv, and A. B. Kucinskas (2001), Gravity field of Mars: A 75th degree and order model, *J. Geophys. Res.*, *106*(E10), 23,377–23,401.

Zhong, S. (2002), Effects of lithosphere on the long-wavelength gravity anomalies and their implications for the formation of the Tharsis rise on Mars, *J. Geophys. Res.*, *107*(E7), 5054, doi:10.1029/2001JE001589.

Zhong, S., and M. T. Zuber (2001), Degree 1 mantle convection and the crustal dichotomy on Mars, *Earth Planet. Sci. Lett.*, *189*, 75–84.

Zuber, M. T. (2001), The crust and mantle of Mars, *Nature*, *412*, 220–227.

Zuber, M. T., and D. E. Smith (1997), Mars without Tharsis, *J. Geophys. Res.*, *102*, 28,673–28,685.

Zuber, M. T., D. E. Smith, S. C. Solomon, D. O. Muhleman, J. W. Head, J. B. Garvin, J. B. Abshire, and J. L. Bufton (1992), The Mars Observer Laser Altimeter investigation, *J. Geophys. Res.*, *97*, 7781–7797.

Zuber, M. T., D. E. Smith, F. G. Lemoine, and G. A. Neumann (1994), The shape and internal structure of the Moon from the Clementine mission, *Science*, *266*, 1839–1843.

Zuber, M. T., et al. (1998), Observations of the north polar region of Mars from the Mars Orbiter Laser Altimeter, *Science*, *282*, 2053–2060.

Zuber, M. T., et al. (2000), Internal structure and early thermal evolution of Mars from Mars Global Surveyor topography and gravity, *Science*, *287*, 1788–1793.

―――――――――――――

F. G. Lemoine, G. A. Neumann, and D. E. Smith, Laboratory for Terrestrial Physics, NASA Goddard Space Flight Center, Code 926, Greenbelt, MD 20771, USA. (neumann@tharsis.gsfc.nasa.gov)

P. J. McGovern, Lunar and Planetary Institute, 3600 Bay Area Boulevard, Houston, TX 77058, USA.

M. A. Wieczorek, Département de Géophysique Spatiale et Planétaire, Institut de Physique du Globe de Paris, 4 Avenue de Neptune, 94107 Saint Maur des Fossés Cedex, France.

M. T. Zuber, Department of Earth, Atmospheric and Planetary Sciences, Massachusetts Institute of Technology, 54-518, Cambridge, MA 02139-4307, USA.